

Generation of mock tidal streams

Mark A. Fardal^{1*}, Martin D. Weinberg¹, Shuiyao Huang¹

¹*Dept. of Astronomy, University of Massachusetts, Amherst, MA, 01003, USA*

Submitted to MNRAS 8 October 2014

ABSTRACT

In this paper we discuss a method for the generation of mock tidal streams. Using an ensemble of simulations in an isochrone potential where the actions and frequencies are known, we derive an empirical recipe for the evolving satellite mass and the corresponding mass loss rate, and the ejection conditions of the stream material. The resulting stream can then be quickly generated either with direct orbital integration, or by using the action-angle formalism. The model naturally produces streaky features within the stream. These are formed due to the radial oscillation of the progenitor and the bursts of stars emitted near pericenter, rather than clumping at particular oscillation phases as sometimes suggested. When detectable, these streaky features are a reliable diagnostic for the stream’s direction of motion and encode other information on the progenitor and its orbit. We show several tests of the recipe in alternate potentials, including a case with a chaotic progenitor orbit which displays a marked effect on the width of the stream. Although the specific ejection recipe may need adjusting when elements such as the orbit or satellite density profile are changed significantly, our examples suggest that model tidal streams can be quickly and accurately generated by models of this general type for use in Bayesian sampling.

Key words: galaxies: kinematics and dynamics – galaxies: interactions – galaxies: haloes – galaxies: star clusters

1 INTRODUCTION

Tidal streams are interesting as potentially very high-precision probes of the mass and shapes of galactic potentials. They also mark the deaths of galactic satellites (which extends the sample of dwarf galaxies we can study), serve as a link between intact galaxies and the smoother halo component, test the predicted population of dark subhalos within galaxy halos, and provide insight into the formation of globular cluster systems.

The methods used for modeling tidal streams range in difficulty from simple orbit fits to use of N -body models. The accuracy of the analysis method should bear some relation to the quality of the observational data and the visible complexity of the stream under discussion. Some tidal streams appear simply as a slightly broadened track, while others appear to have multiple components (as in the case of the Sagittarius stream, Belokurov et al. 2006 and Sohn et al. 2014) or density variations in excess of random noise (as in the case of Pal 5, Odenkirchen et al. (2003)). Obtaining a fit to a given stream can be useful, but it is more informative to obtain confidence intervals for parameters of interest, which usually involves Bayesian sampling techniques that require many stream-model comparisons.

Some recent papers have proposed stream analysis methods that avoid specific modeling of the tidal disruption process (Price-Whelan et al. 2014; Sanderson et al. 2014). These methods work well when given high precision information on all six dimensions of phase space. But in most cases, and especially when some dimensions are unconstrained by observations, it seems useful to have the analysis method incorporate more information on the way the stream stars are released from their progenitor. This will be even more advantageous in cases where substructure from radial oscillations is detectable in the stream.

Among those methods that actually model tidal streams for comparison to data, N -body simulations are the most accurate way to treat the problem, but also the most expensive, as well as in some ways the most difficult to interpret. Therefore their application has been limited to date (Howley et al. 2008; Fardal et al. 2013). Simpler methods generate a single track to be fitted to the stream. Many authors have simply assumed that the stream follows the orbit of the progenitor, which is a useful approximation but not a generally correct one. Other methods for generating a stream track include the streakline techniques of Varghese et al. (2011) and Küpper et al. (2012), which release particles at constant intervals. These methods are most useful when the progenitor is slowly and continuously disrupting. Other, more approximate methods for estimating the stream track which

* E-mail: fardal@astro.umass.edu

are useful in different circumstances have been used as well (Johnston 1998; Fardal et al. 2006).

Action-angle methods, as used by numerous authors (Helmi & White 1999; Eyre & Binney 2011; Sanders & Binney 2013a,b; Bovy 2014; Sanders 2014) result in the clearest conceptual picture of the dynamical structure of the stream. However, these methods are equivalent in their function to doing orbit integrations in the host potential, and therefore still require accurate release conditions for the particles. Some recipes have been proposed within this context (Eyre & Binney 2011; Bovy 2014), but they have not yet been shown to be precise or generally applicable. A separate issue is that computation of action-angle coordinates requires separable potentials for maximum efficiency, and if that is not possible actions and angles may not exist globally for the given potential.

Recently, Gibbons et al. (2014) and Bonaca et al. (2014) have both proposed modeling the streams using sprays of particles released from the satellite and integrated within the host potential.¹ Gibbons et al. (2014) assert the potential of the satellite must be included to make this feasible. Using somewhat different release conditions, Bonaca et al. (2014) find it unnecessary to include the satellite potential. However, the testing presented for their method is quite limited and one may question its general applicability. Both these prescriptions also assume a constant progenitor mass, despite the fact that stream creation implies an ongoing loss of mass.

In this paper, we test a recipe for stream particle ejection against a sample of N -body simulations. We judge our recipe for release conditions by whether it reproduces distributions of actions and frequencies computed from the simulations, since these are the quantities most relevant to the observed structure of the stream. To make this comparison practical, we conduct all the test simulations in an isochrone potential, since the actions and frequencies in this potential are analytic functions of the positions and velocities. To keep the testing simple, our progenitor satellites are simple one-component models such as might be expected for globular clusters. The recipe can be generalized to more complex cases with minor changes.

In Section 2, we review the basic properties of tidal streams, and define the parameters controlling the way stream stars are released. We describe the sample of simulations in Section 3. In Section 4, we constrain the mass loss recipe which determines how many stream stars are created and at what times, as well as the release parameters, which determine the orbits of the stars once created. Section 5 illustrates the performance of the generated streams. In Section 6, we discuss the wider applicability of our results and compare to some other recent stream modeling, and we summarize our results in Section 7.

¹ Very recently, N. Amorisco posted a preprint covering some of the issues discussed here (astro-ph/1410.0360).

2 THE BEHAVIOR OF TIDAL STREAMS

2.1 Stream generation in phase space

Although descriptions in other coordinate bases are often possible, the most universal way of describing a tidal stream is as a collection of tracer particles thrown off a satellite as it orbits its host potential, with those particles integrated in position-velocity space (phase space) under the combined influence of the host and the satellite. In the case of a circular orbit within a spherical potential, a necessary condition for particles to escape from a satellite at radius r is that they exceed the tidal radius (or Jacobi radius), which can be written as

$$r_{\text{tidal}} = \left(\frac{m_{\text{sat}}}{f M(< r)} \right)^{1/3} r \quad (1)$$

where M is the mass of the host in which the progenitor orbits, and

$$f \equiv 1 - \Omega^{-2} d^2 \Phi / dr^2 = 3 - d \ln(M) / d \ln(r) \quad (2)$$

and $\Omega = V_c(r)/r = (GM(< r)/r^3)^{1/2}$ is the circular angular speed (Binney & Tremaine 2008). Note that $f = 3$ for a Kepler potential and $f = 2$ for a logarithmic halo. We assume $m_{\text{sat}}(< r_{\text{tidal}}) \approx m_{\text{sat}}$, which is commonly satisfied at least after tides have had a chance to strip the outermost particles. Even in this case the escape process is not simple, and much attention has been devoted to the orbits of stars in the classic point-mass Hill problem and its generalizations (Heggie 2001a). Stars escape into leading and trailing streams from near the Lagrange points located at $\pm r_{\text{tidal}}$ from the satellite along the radial vector to the host center.

For an eccentric orbit, there is no known rigorous definition of a tidal radius, but the concept is still useful in estimating the amount of mass loss. We continue to define the tidal radius by equation 1, where $\Omega = V_c(r)/r$ is the circular angular speed. Thus the generalized tidal radius depends only on the potential, satellite mass, and radius. Note that some authors cited here instead set Ω in equation 2 to be the actual angular velocity v_t/r of the satellite, where v_t is the tangential velocity.

If the stripping is not too violent, the stars again escape into well-separated leading and trailing streams from near the Lagrange points. A greater eccentricity of the orbit leads to a disruption rate more strongly peaked near pericenter. If the tidal forces are strong enough, the entire satellite may disrupt at once, giving a continuum of ejected particles from leading to trailing.

2.2 Stream behavior in action-angle space

The *simplest* description of tidal streams occurs when the stream stars can be described by action-angle variables (Helmi & White 1999; Eyre & Binney 2011; Bovy 2014). In these coordinates the stars behave as free particles, at least if we ignore the continued effect of the satellite as in the previous subsection. There are certainly cases where an action-angle description is *not* possible. For example, the stars may become unbound from the host potential, and hence cease to execute oscillatory behavior. When the potential is irregular, as is true for almost any realistic galaxy

potential, actions do not truly exist. However, the action-angle description continues to be useful, if only as an approximation. For example, in a spherical halo whose potential is flattened by the disk, an action-angle computation is likely to be effective as long as the orbital plane precession frequency remains much smaller than either of the radial or azimuthal frequencies.

Here we summarize the action-angle approach, mostly adopting the notation of Bovy (2014). We take the current time at which the stream is observed to be $t = 0$. Stars are released from the progenitor at positive lookback times t_s , (times $t = -t_s$). The Hamiltonian is expressed in terms of the actions and is independent of the angles. Therefore the actions are constant with time, and the gradient of the Hamiltonian in action space gives the time derivative of the angles, $\dot{\theta} = \partial H / \partial \mathbf{J} = \boldsymbol{\Omega}(t_s) = \text{constant}$, implying $\theta = \theta(t_s) + \boldsymbol{\Omega} t_s$. With reference to the progenitor's quantities $\theta^{(p)}$, $\boldsymbol{\Omega}^{(p)}$, the offsets are measured as $\Delta\theta = \Delta\theta(-t_s) + \Delta\boldsymbol{\Omega} t_s$, $\Delta\boldsymbol{\Omega} = \text{constant}$. Normally, we can assume that $\Delta\boldsymbol{\Omega}$ is small (comparable to r_t/r , so that a linear expansion of the frequencies is applicable. This will be adequate unless the progenitor mass exceeds say 10^{-3} of its host mass (Bovy 2014), in which case nonlinear terms can become important. Normally, $\Delta\theta(t_s)$ is small as well, so that the properties of $\Delta\theta$ are dominated by the second term. However, in rare cases, the orbit may be close enough to circular so that the emitted stars are “trapped” near pericenter and apocenter, rather than following the phase of the progenitor. We will return to this case later.

The orbital behavior of the stars must be coupled with a description of the rate at which particles are released into the stream, and their initial action and angle offsets. Some authors focus on models with a continuous release of particles from an initial time to the present (we call this the “leak case”). If the mean frequency of particles released into the stream is $\boldsymbol{\Omega}^m$, then this forms a stream track governed by $\Delta\theta \approx \Delta\boldsymbol{\Omega}^m t_s$ where t_s takes on a range of values. Some authors instead focus on streams formed instantaneously at a single disruption time t_d (“burst case”), in which case the track is instead described by $\Delta\theta \approx t_d \Delta\boldsymbol{\Omega}$ where here $\Delta\boldsymbol{\Omega}$ takes on a range of values. The formalism of Bovy (2014) has a smooth disruption starting at an finite lookback time t_d , so the stream track derived there smoothly interpolates between these two limits at a scale $\Delta\theta \sim \Delta\boldsymbol{\Omega}^m t_d$, resembling the leak case at smaller angles and the burst case at larger ones.

Unless the orbit is nearly circular, we expect the stars to be released predominantly but not entirely near pericenter. If the progenitor manages to survive its first pericenter intact, the release model should actually resemble a combination of the leak case with a series of overlaid bursts. The ejection from some satellites might have finite starting and ending times, though in this case we expect the scale of the frequency offsets to change throughout the lifetime of the progenitor.

Although the distribution in action-action space shows a complex bow-tie shape (Eyre & Binney 2011), the distribution in frequency-frequency space is nearly diagonal (see Bovy 2014). The distance along the diagonal is correlated generally speaking with the magnitude of the action offset (or more specifically, nearly with the particle energy; Johnston 1998). This leads to two qualitatively different types of

“tilts” between the stream and the progenitor orbit. First, for particles released in a single burst, the action and frequency offset are strongly correlated. Particles with high energy lag behind in the orbit, while particles with low energy speed ahead. This creates a tilt between the stream and the orbit.

The second kind of tilt results from the fact that the narrow diagonal distribution of particles in frequency space is in most cases not pointed exactly along the frequency vector of the satellite (Eyre & Binney 2011), though in general it is at least close. One factor in this misalignment angle is that for typical galactic potentials the ratio of radial to azimuthal frequencies tends to decrease for stars executing larger-radius, higher-energy orbits. Therefore, regardless of whether particles are released in a burst or leak slowly, the angle vectors tends to extend along a line misaligned from the frequency vector.

The action-angle and angle-angle tilts are generally both in operation, so that it is not always simple to guess where the stream will lie in real space relative to the orbit without detailed calculations. However, in young streams (less than a few orbits), we can usually expect the action-angle tilt to dominate the offset between the stream and the orbit. The opposite is true for old streams, say those that have executed tens of orbits. Naturally, an ejection recipe that correctly reproduces the distribution in release time and action space should correctly reproduce the effect of both of these tilts.

2.3 Substructure in the stream

Orbits of galactic satellites and globular clusters are typically highly eccentric. Ratios of apocenter r_a to pericenter r_p of about 4 are typical, as expected for mildly radial tracer populations in typical halo potentials (van den Bosch et al. 1999). Since tidal forces are a major influence on the mass loss rate, and these forces depend on the radius to a high power (r^{-3} for Kepler or r^{-2} for a logarithmic halo), we can expect the mass loss to proceed as a series of bursts, at least for the progenitors that do not fall apart in the first encounter with their host. Thus most tidal streams can be expected to fall somewhere between the extremes of “burst” and “leak” behavior. This is one possible source of substructure within the stream.

Küpper et al. (2008) and Just et al. (2009) drew attention to the substructure in tidal streams. These models used progenitors on circular orbits, but subsequent papers (Küpper et al. 2010, 2012) involved eccentric orbits. A point possibly obscured in these papers is that the origin of substructure in these two cases is fundamentally different. In the circular case, the substructure arises from clumps of stars at particular values of their *current* radial angle, i.e. the pericentric locations of the stream stars. This is only possible because the circular case is in the “trapped” regime mentioned above: the phase of the emitted stars in the trailing (leading) tail is always near pericenter (apocenter), rather than continuously increasing following the phase of the progenitor. In the more general case, the substructure is characterized by particular values of the radial angle at *emission*, not its current value. This behavior is clearest in action-angle space, where the stars move in their tori with constant angular velocity. In real space, the streaky features (as do all parts of

the stream) have their density enhanced at apocenter, due to the slower motion of the stream particles there. The density seen in the phase-space stream is a combination of these two effects.

The dividing line between the trapped and untrapped regimes occurs when the stars emitted at apocenter are placed on circular orbits. The conditions for this can be found using the epicyclic approximation. We write the azimuthal frequency as Ω and the radial frequency as κ . Let us suppose that stars are ejected at a position offset by $k_r r_{\text{tidal}}$ from the satellite, with a tangential velocity offset by $k_{v\phi} \Omega r_{\text{tidal}}$ from the satellite. To place the ejected stars on circular orbits, the radial epicycle amplitude X of the satellite must take the value $X = (2\Omega^2/\kappa^2)[k_{v\phi} - (1 + d \ln \Omega / d \ln R)k_r]r_{\text{tidal}}$, neglecting second-order terms. For a flat rotation curve this simplifies to $X = k_{v\phi} r_{\text{tidal}}$. In other words, the epicyclic radius dividing trapped from untrapped regimes is of order r_{tidal} , with the exact value depending on the values of k_r and $k_{v\phi}$ (which will be investigated in section 2.4 below) and the rotation curve. This means that only nearly circular orbits (with $r_a/r_p \approx 1 + 2X$) can be in the trapped regime. For globular clusters with a mass $\sim 10^{-6}$ that of their host, this demands an epicyclic radius $\sim 10^{-2}$ that of the orbital radius, or a radial action $J_r < 10^{-4} L_z$. For representative dwarf galaxies, this criterion rises to $J_r < 10^{-2} L_z$. Thus the trapped regime probes a negligibly small region of phase space.

In the more common untrapped case which occurs for larger eccentricity, the clumps seen in simulations spaced fairly evenly in phase along the stream cannot be due to their current radial phase. Instead, they are determined by the radial phase at ejection, and have two simultaneous causes: the variation of the mass loss rate with radial phase, and the correlation of action and frequency values with radial phase. The following example illustrates these stream features.

Figure 1 (upper panel) shows the particle locations for one of the simulations described in Section 3. This simulation is shown at the fourth apocenter passage. We can see streaky features within the stream, which increasingly overlap as we go outwards from the satellite. If we convert to action-angle space (lower panel), the origin of the streaks is clearer. We can see that the streaks correspond to bursts of particles released near pericenter, as indicated by the color coding. Even though one might expect apocentric clumps of particles, due to the long time that the progenitor spends near apocenter, these clumps do not appear to exist simply because few particles are released around apocenter. Clearly, one must take both the variation in release rate and the dispersion in the release conditions into account to model the streaks.

In action-angle space, the inclination of the streaks has a consistent sign across both the leading and trailing streams. The tilt of the streaky features in action-angle space is $\Delta\Omega = t_s^{-1} \Delta\theta$, thus going to zero for large lookback times. This tilt pattern translates fairly well to the real-space view as well. In general streaky features are inclined such that their leading part points inward and their trailing part outwards when compared to the mean stream path. Thus streaky features provide an indicator of the stream's direction of motion, which may be useful in cases where it is not instantly apparent from other characteristics such as

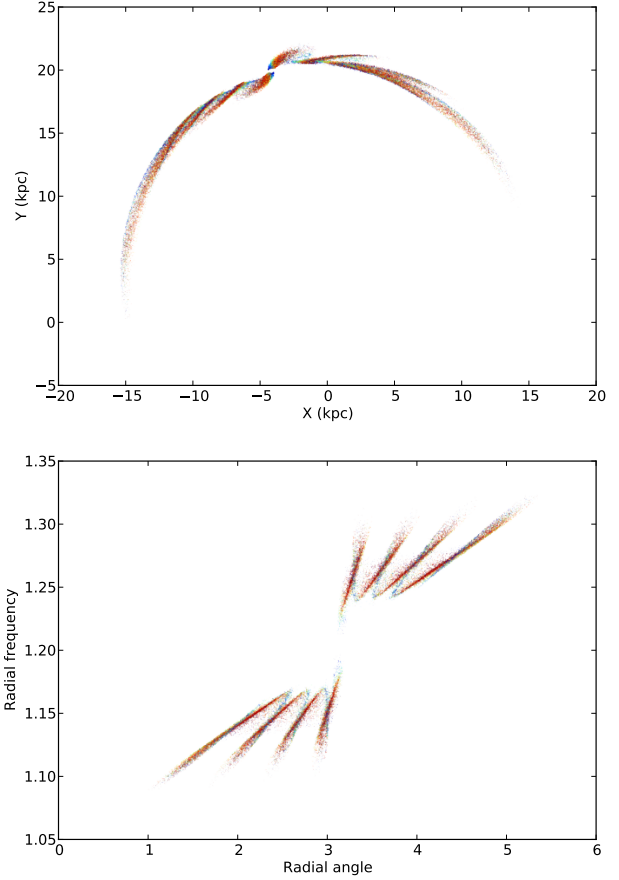


Figure 1. Top: particle positions in the X - Y plane in the `orb1.5_m6.0_fat` run, described in section 3 and Table 1. Only unbound particles are shown, at the fourth apocenter passage of the satellite. Color indicates the cosine of the estimated release phase of the satellite, with red marking pericenter and blue apocenter. Bottom: radial frequency versus radial angle, shown at the same time as the upper panel.

kinematic measurements or leading-trailing stream asymmetries.

Counting the streaky features provides a simple indication of the number of pericentric passages the progenitor has undergone, and thus the timescale over which the stream stars have been disrupted. The spacing between the midpoint of the streaky features in angle space is $\Delta\Omega^m(r_{\text{peri}})T_{\text{radial}}$, constant in time, though the visibility decreases as time goes on due to the increasing alignment and overlap of the features. In real space, this spacing will fluctuate as the stream moves from apocenter to pericenter and its angular speed varies. The stream tail at $|\Delta\theta| > |\Delta\Omega^m|t_d$ discussed by Bovy (2014) is in essence the oldest streaky feature in the stream, caused by the burst of particles released at the initial pericenter.

2.4 Parameterization of the ejection model

It would be useful to be able to model the ejection from the satellite without performing a full N -body simulation. To model the location of the stream correctly, we need an accurate recipe for ejecting particles from the satellite. This

recipe must supply both the ejection rate from the satellite and the properties of the ejected particles at the time of ejection. Simple models for the ejection rate could assume a single burst, multiple bursts, or a continuous leak of particles. A more realistic model will assign a distribution of ejection times within a radial cycle.

After escaping from the satellite the stars feel its influence diminish rapidly, but the influence of the satellite (and perhaps of the tidal debris) does not stop entirely at the tidal radius for any star (as examined in Choi et al. 2007). This influence is felt especially long for stars that lap the progenitor in azimuth, or those that have orbital resonances with it, and also in cases where the progenitor has a large mass and thus affects even particles at large angular separations from it. Thus it is not quite correct to examine the conditions of particles crossing the tidal radius and conclude that they determine the final tidal stream structure. However, for small progenitor masses we can still specify the behavior of stars fairly well in terms of orbits in the host potential alone, when ejected from *some* location near the satellite with *some* velocity (not necessarily the actual velocity at that point). Let us rewrite these ejection conditions as follows, using polar coordinates (r, ϕ, v_r, v_t) .

$$r = r_{\text{sat}} + k_r r_{\text{tidal}} \quad (3)$$

$$\phi = \phi_{\text{sat}} + k_\phi r_{\text{tidal}}/r \quad (4)$$

$$v_r = v_{r,\text{sat}} + k_{vr} v_{r,\text{sat}} \quad (5)$$

$$v_t = v_{t,\text{sat}} + k_{v\phi} V_c(r) r_{\text{tidal}}/r \quad (6)$$

$$z = k_z r_{\text{tidal}}/r \quad (7)$$

$$v_z = k_{vz} V_c(r_{\text{sat}}) r_{\text{tidal}}/r. \quad (8)$$

These forms are similar to some previous models, in particular the streakline models of Varghese et al. (2011) and Küpper et al. (2012). The primary difference between those two models is the treatment of the tangential velocity of the ejected particles. Varghese et al. (2011) assume a physical velocity equal to that of the satellite ($k_{v\phi} = 0$), while Küpper et al. (2012) assume an *angular* velocity equal to that of the satellite ($k_{v\phi} = 1$, for the $k_r = 1$ assumed there).

In principle the six parameters $k_r, k_\phi, k_{vr}, k_{v\phi}, k_z, k_{vz}$ could be constants, functions of time, or random samples from distributions that depend on time; we will assume the latter. Along with other authors we will set

$$k_\phi = k_{vr} = 0 \quad (9)$$

and test whether this gives a reasonable model for the ejecta. We assume the other parameters are either constants or are described by Gaussian distributions. This is unlikely to be accurate in the extremes of the distribution, but in this paper we are only aiming for an approximation that reproduces the typical dispersions.

The ejection conditions must be coupled with a description of the ejection rate, which will be a function of the satellite’s structure and orbit. With these two ingredients, we can integrate particles in the host potential to predict the phase-space properties of the stream.

3 SIMULATION SET

To constrain our particle-spray model, we conduct a set of N -body simulations. Our goal is to demonstrate that a rea-

Table 1. Test simulations

Name	r_p (kpc)	r_a (kpc)	r_a/r_p	T_{rad}	m_{sat}	f_t
orb1.2.m6.0	16.92	20.30	1.2	400.0	10^6	0.8
orb1.5.m6.0	14.88	22.31	1.5	400.0	10^6	0.8
orb2.0.m6.0	12.40	24.77	2.0	400.8	10^6	0.8
orb3.0.m6.0	9.24	27.72	3.0	400.0	10^6	0.8
orb5.0.m6.0	6.12	30.51	5.0	400.2	10^6	0.8
orb1.2.m6.0.fat	16.92	20.30	1.2	400.0	10^6	1.2
orb1.5.m6.0.fat	14.88	22.31	1.5	400.0	10^6	1.2
orb2.0.m6.0.fat	12.40	24.77	2.0	400.8	10^6	1.2
orb2.0.m6.0.thin	12.40	24.77	2.0	400.8	10^6	0.5
orb3.0.m6.0.thin	9.24	27.72	3.0	400.0	10^6	0.5
orb5.0.m6.0.thin	6.12	30.51	5.0	400.2	10^6	0.5
orb7.0.m6.0.thin	4.54	31.77	7.0	400.0	10^6	0.5

sonable model can be derived for some range of satellites and orbits, but we do not expect that this model will be applicable to all situations. All simulations take place within an isochrone host potential, so we can calculate actions and angles easily. Our simulations use relatively diffuse satellites where tidal forces are responsible for the disruption. This stands in contrast to many models of globular cluster evaporation, where ejection is often dominated by internal relaxation processes and stellar mass loss; these must be modeled either by collisional N -body simulations or Fokker-Planck codes (Aarseth & Heggie 1998; Chernoff & Weinberg 1990; Murali & Weinberg 1997; Gnedin & Ostriker 1997; Takahashi & Portegies Zwart 2000; Lamers et al. 2010; Gieles et al. 2014). Thus the specific fits derived here may not be applicable to all globular clusters. However, roughly half of MW clusters (preferentially at small galactocentric radii) have destruction time scales dominated by tidal forces as opposed to relaxation (Heggie 2001b). The observable globular streams may be predominantly those where strong tidal forces induce rapid leakage of stars, so our models are not necessarily inapplicable to some globulars as well as dwarf galaxies.

Our simulations are of course scale-free, but for comparison to observed systems we choose a unit system where the isochrone potential has mass $M = 2.852 \times 10^{11} M_\odot$, and scale length $b = 3.64$ kpc. This follows the choices of Eyre & Binney (2011) and provides a rotation velocity similar to that of the Milky Way for radii near that of the Sun. All orbits are chosen to have orbital periods 400 Gyr, and the r_a/r_p span a range 1.2–7.0. We use spherical King (1966) model satellites with $W = 3$ (i.e., not very concentrated). The simulations are listed in Table 1, and are named according to the orbit, mass, and scale length.

We place the model satellites at the apocenter of their orbit. We set the initial outer or “tidal” radius of the King model to be a specified fraction f_t of the tidal radius at *apocenter*:

$$f_t \equiv r_{\text{King66}}/r_{\text{tidal}}(r_{\text{apo}}). \quad (10)$$

The tidal radius at pericenter can be inferred from Table 1 and equation 1, but in most cases it is inside the initial model outer radius, inducing significant mass loss at each pericenter.

We run the test simulations until the time reaches 4.3 Gyr. We save snapshots every 10 Myr. We track the position of the satellite as a function of time and convert it to action-

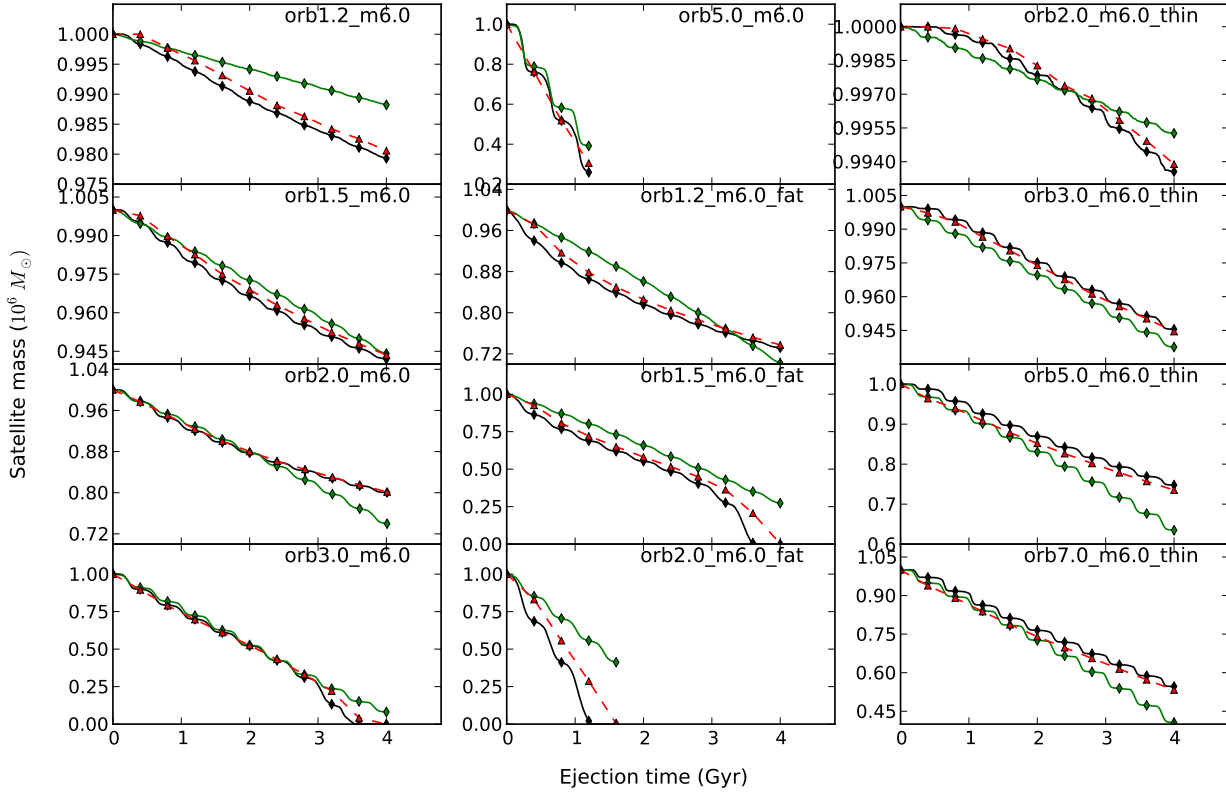


Figure 2. Satellite mass as a function of time. Black: mass within tidal radius measured from simulations. Wiggles illustrating periodic mass loss enhancements are clearly visible. Red: predicted mass at successive apocenters, obtained by truncating actual simulation structure at the previous apocenter near the pericentric tidal radius, as discussed in the text. Green: mass predicted from the full mass loss model, which uses only the initial satellite orbit, mass and structure as inputs. Small symbols denote mass at apocenter.

angle variables. In some cases the orbital frequencies seem to deviate slightly from the expectations based on the initial orbit, most likely due to interaction of the satellite with its own tidal debris (as expected from Choi et al. 2007). Thus we compute corrected frequencies from the measured satellite positions, and use the new frequencies to initialize a finely spaced lookup table for each satellite’s position and velocity as a function of simulation time.

For each particle outside the tidal radius at the final snapshot, we estimate the ejection time from its action-angle coordinates. Using this to estimate a useful starting time, we compute the orbit of the particle backwards in time between snapshots in a two-body time-dependent potential, using the lookup table to compute the satellite position. We use this to infer a more accurate ejection time from the satellite, as defined by the time at which the particle crosses the tidal radius. We then save the position and velocity of the particle and satellite. In some cases this procedure fails. For some cases, the radial and azimuthal angles do not predict the same ejection time. Many of these are near the satellite and some have probably interacted multiple times with the satellite. Some other failures occur when the satellite is falling apart rapidly and the point mass approximation fails. When the refined approximation fails, we find the ejection time using a linear interpolation of the radial distance from the satellite at snapshots.

4 DERIVING A MASS LOSS MODEL FOR TIDAL STREAMS

4.1 Mass loss model

To form a complete model of the tidal stream, we must model the rate of mass loss in addition to the conditions of the ejected particles. We will do this by comparison to the simulations in section 3. The first step in constructing the mass model is to specify the satellite mass at subsequent apocenters. Earlier work on satellites of various types has suggested that the evolution of the satellite mass and density profile follow quite predictable tracks, given only the initial orbit and structure (Hayashi et al. 2003; Peñarrubia et al. 2008). In our simulation set, we find that the satellite mass at the next apocenter can be reproduced quite well in most cases simply by truncating the apocentric profile at 0.9 times the tidal radius at pericenter. Figure 2 illustrates the results of this procedure. The red curve represents the satellite mass predicted at each apocenter, based on truncating the satellite structure of the previous apocenter. This agrees well with the simulation results shown by the black curve.

However, it is not sufficient for our model to predict the mass using the actual, evolving structure of the simulated N -body satellite, as we want to dispense with N -body simulations altogether. We find that after the first pericentric passage, the radial profiles of satellites that do not disrupt altogether are reasonably well described by Einasto profiles,

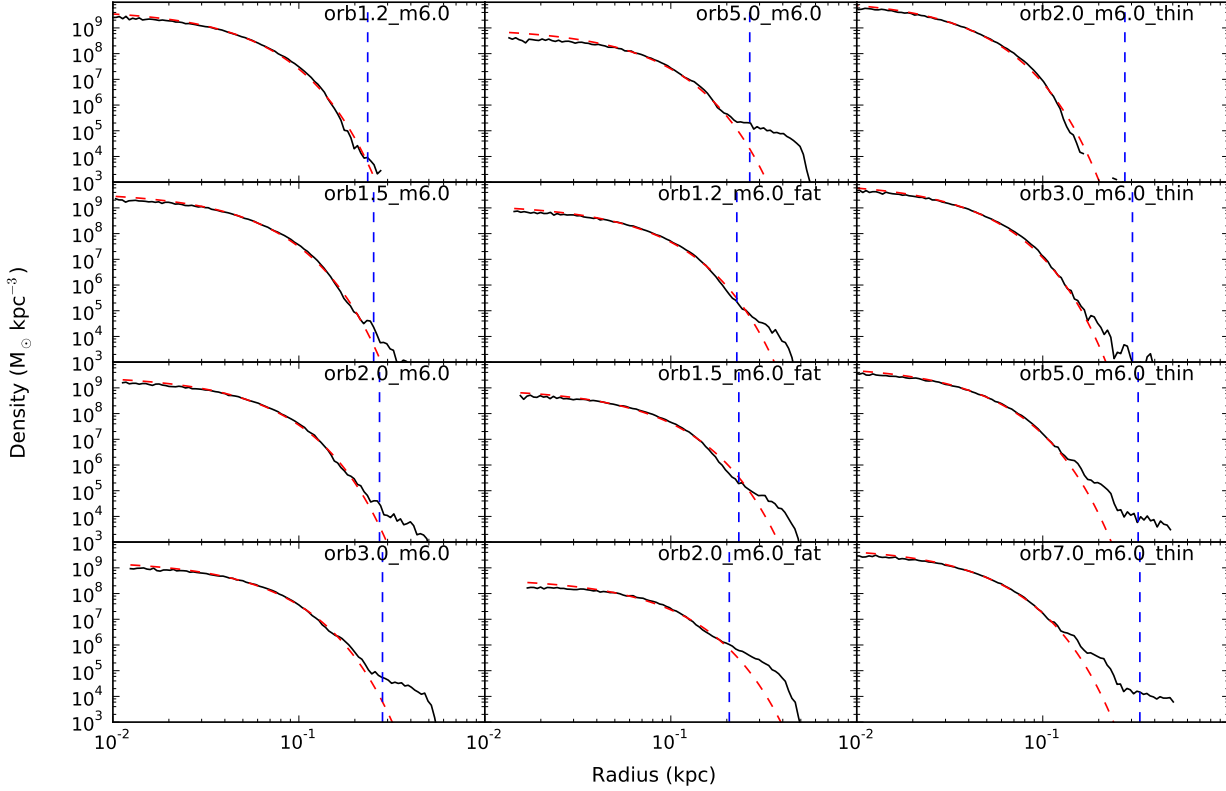


Figure 3. Radial density profiles, as measured at the third apocenter. Black: profile measured from simulation, discarding any formally unbound particles. Red: profile generated from mass loss model using current mass, initial mass, and initial density profile. Blue: tidal radius at apocenter.

as shown in Figure 3. In this figure, we only include those particles that are formally bound to the satellite, as defined by the relative velocity and potential from the satellite and its debris (and ignoring the tidal force). We write the Einasto profile in the form

$$\rho(r) = \frac{(2\mu)^{3\mu} m_{sat}}{4\pi r_{sc}^3 \mu e^{2\mu} \Gamma(3\mu)} \exp \left\{ -2\mu \left[\left(\frac{r}{r_{sc}} \right)^{1/\mu} - 1 \right] \right\} \quad (11)$$

so the index μ resembles the n in the related Sersic profile. Here r_{sc} is the radius at which the logarithmic slope of the density equals the isothermal slope -2 . For this profile, the cumulative mass is given by

$$M(< r) = m_{sat} \gamma \left[3\mu, 2\mu(r/r_{sc})^{1/\mu} \right] \quad (12)$$

where γ is the normalized incomplete gamma function.

Furthermore, we find that the radial scale evolves little over the course of the simulation, while the density scale drops significantly. Therefore we simply assume the radial scale is fixed at $r_{sc} = 0.2r_{outer}$, where r_{outer} is the initial outer or “tidal” radius of the King model. The density scale then simply scales with the initial mass. The optimal μ varies slightly between runs and snapshots, but for simplicity we keep it fixed at $\mu = 0.9$. In other words, the density profile is fairly close to exponential.

The resulting fits are shown in Figure 3. At large radius the tidal debris shows some complicated structure which cannot be modeled by a simple profile, but within a radius containing most of the mass the fit is fairly good. Once we

have a sequence of apocenter masses, this determines the amount of mass lost over each radial cycle, and this prediction is shown in Figure 2.

As our simulations take place in a spherical potential, we include only the effects of “bulge shocking” but neglect those of “disk shocking”. The performance of our recipe should be checked particularly in cases where satellites pass directly through the disk of the host, as these may require an enhanced degree of mass loss which is dependent on the full details of the orbit rather than just the oscillations in radius.

To determine the variation of mass ejection rate within this cycle, we first define the “acceleration gradient” as

$$g_a \equiv \Omega^2 - d^2\Phi(r)/dr^2, \quad (13)$$

where $\Omega = V_c(r)/r$ is again the circular frequency. This quantity represents the second derivative with radius of the effective potential, for a circular orbit, and thus measures the strength of the tidal force. (Note $g_a = \Omega^2 f$). We then compute the ratio of this quantity at apocenter and pericenter,

$$R_{acc} \equiv \frac{g_a(r_{peri})}{g_a(r_{apo})} \quad (14)$$

We use R_{acc} as our measure for the variation of the tidal forces over a radial oscillation.

We use the following analytic form to define the ejection rate as a function of radial phase θ_r :

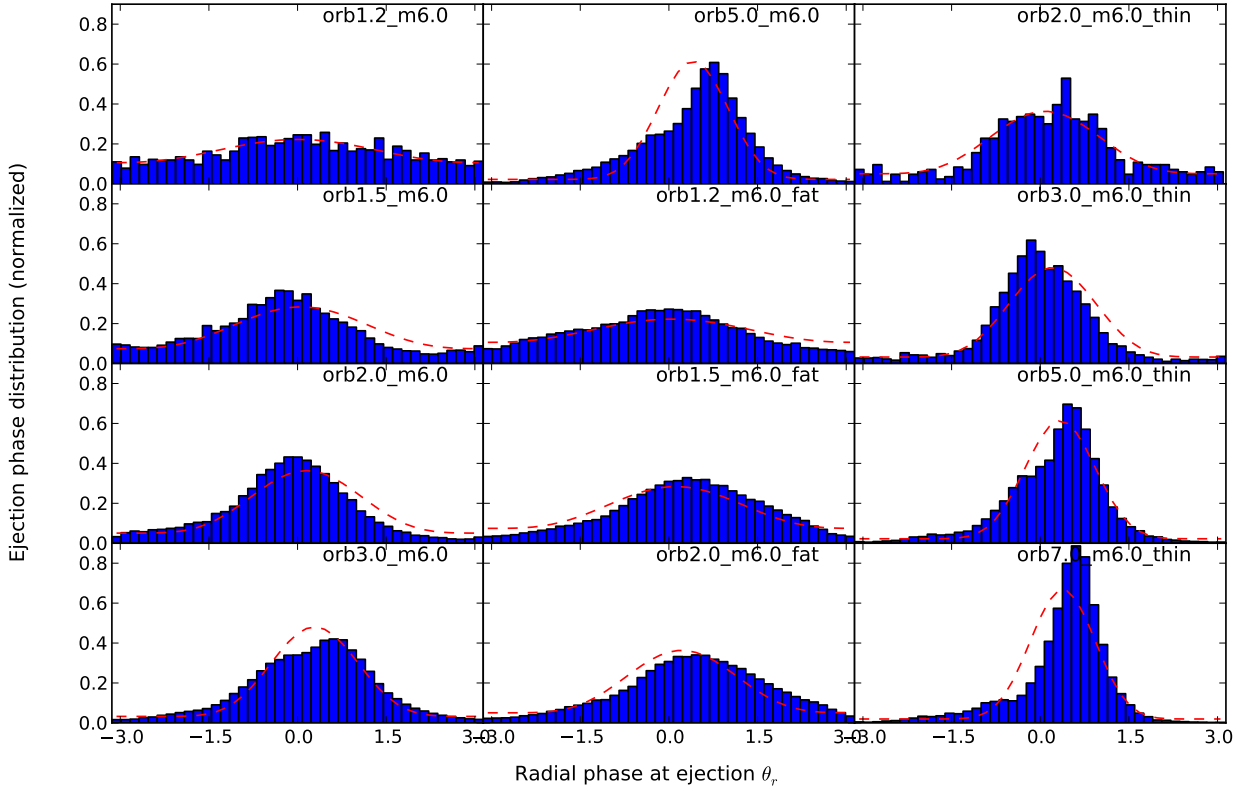


Figure 4. Distribution of mass loss in ejection radial phase. Blue histograms: distribution measured from simulations, as measured from crossing at one tidal radius. Red: model specified by orbit and initial size, as in text. Clearly the model captures the overall peaky behavior while ignoring some of the finer structure.

$$\frac{dM}{d\theta_r} = A \left(1 + (r_{ej} - 1) \left[\frac{1 + \cos(\theta_r - \theta_{mid})}{2} \right]^\alpha \right) \quad (15)$$

With this form, the ratio of ejection at peak to trough is r_{ej} . The normalization and cumulative distribution of this form can be calculated using beta functions (complete and incomplete respectively).

We then set the parameters in this expression using

$$r_{ej} = \exp(1.4 R_{acc}^{3/4}) \quad (16)$$

$$\alpha = R_{acc}^{0.55} \quad (17)$$

$$\theta_{mid} = -0.1 + 0.7 \frac{f_t R_{acc}}{7 + f_t R_{acc}} \quad (18)$$

These forms were determined by comparison with the distribution of ejection phase in the simulations (Figure 4).

These parameter expressions are sufficient to approximate the variation of emission rate with satellite orbital phase, to the degree required to specify reasonable models. They are not well justified physically so should be checked in cases that are far from Note that the rate of particle emission peaks substantially after pericenter in some cases.

With these specifications, we can now model the particle emission from the simulated satellite. We first determine the number of particles to be ejected between subsequent apocenters, then randomly sample from equation 15 using the rejection method, which generates a sequence of ejected particles. The mass in the satellite is determined by the analytic formula for the cumulative ejected mass.

4.2 Ejection model

The last step is to specify the orbital release conditions of the ejected particles. We determine this by comparison with the final actions and frequencies of the ejected particles in the simulations as a function of radial phase at ejection. Since we are using spherical isochrone potential, the azimuthal and vertical frequencies are degenerate, so we focus on the behavior in 4-dimensional action-angle space.

We specify the release using equations 3–6, setting $k_\phi = 0$, $k_{vr} = 0$, and choosing k_r , $k_{v\phi}$ to be constants. We began by examining the predictions of the Varghese et al. (2011) and Küpper et al. (2012) initial conditions discussed previously. The mean action and frequency offsets generated by the two initial conditions are fairly similar when averaged over a radial cycle, but the variation of the frequencies with phase is much stronger using the Küpper initial conditions. We optimized the choice of constants essentially by eye. The mean values for the k constants are

$$\bar{k}_r = 2.0, \quad (19)$$

$$\bar{k}_{v\phi} = 0.3. \quad (20)$$

This is closer to the Varghese conditions than the Küpper condition, the choice of which tends to make the frequencies vary too much with orbital phase. The optimal parameters appear to vary slightly between simulations, but not strongly enough for us to justify a more complex choice.

However, Figures 5 and 6 show that the *dispersion* in

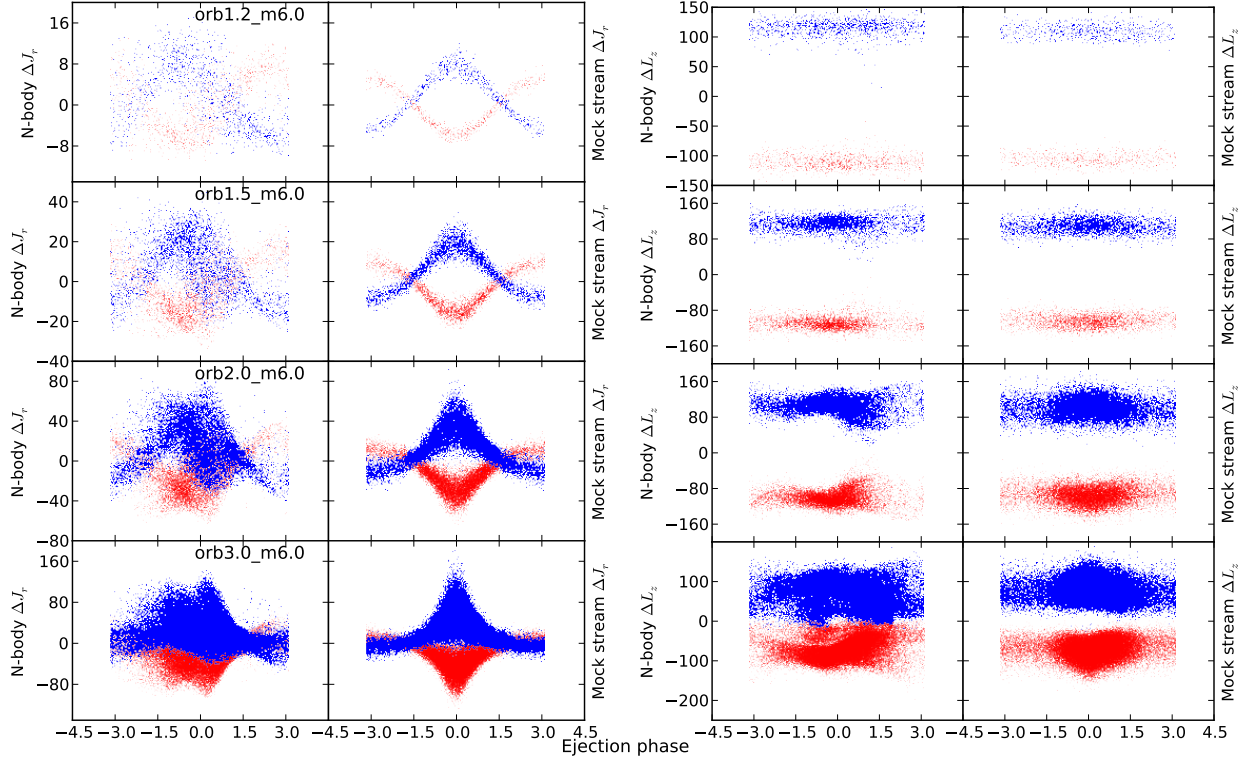


Figure 5. Actions of stream stars. First two columns show J_r , second two show L_z . Both are given in units of kpc km s^{-1} . In each pair of columns, simulation results are on the left and results from the mass loss model on the right.

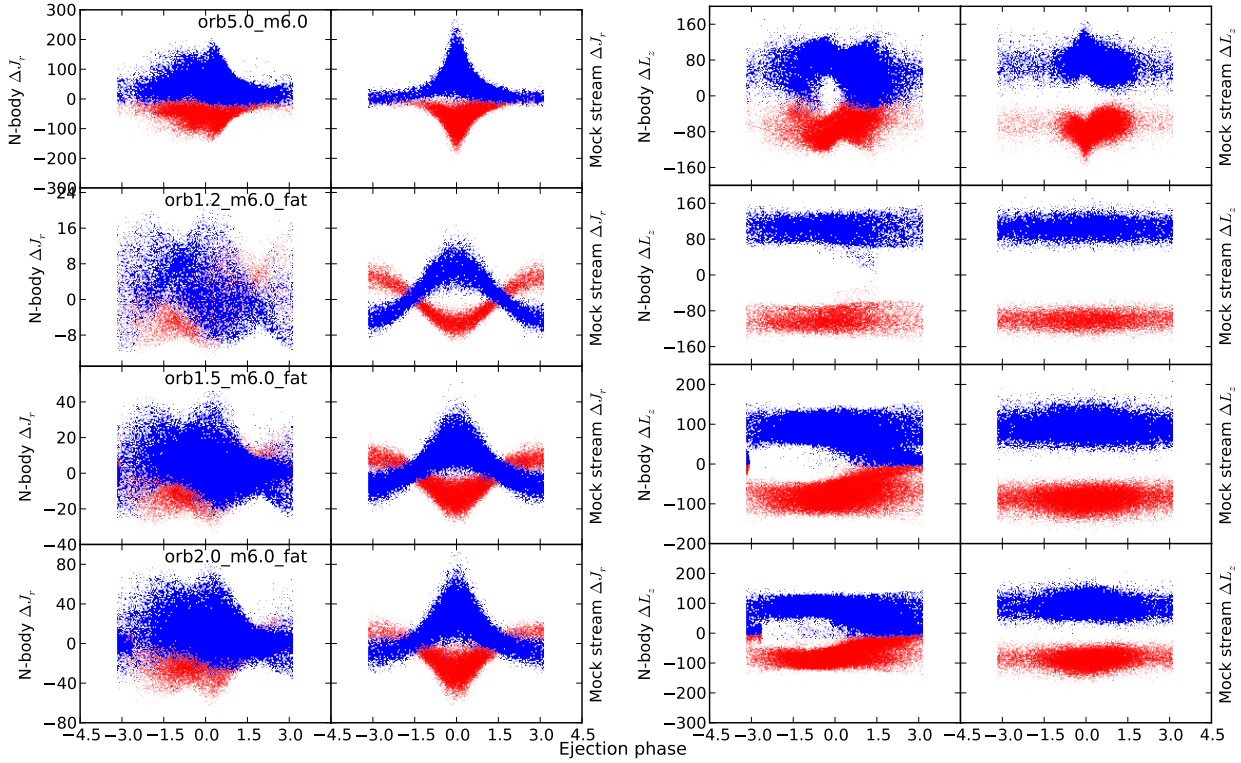


Figure 5 – continued

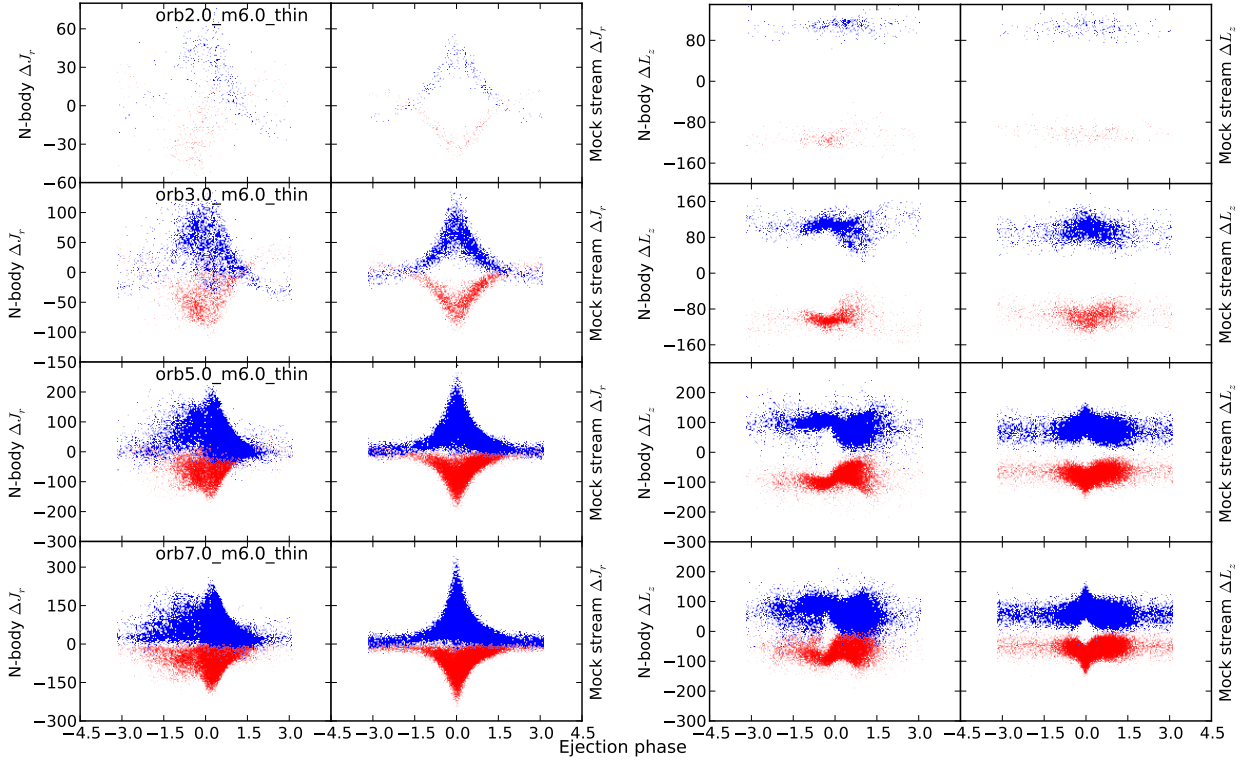
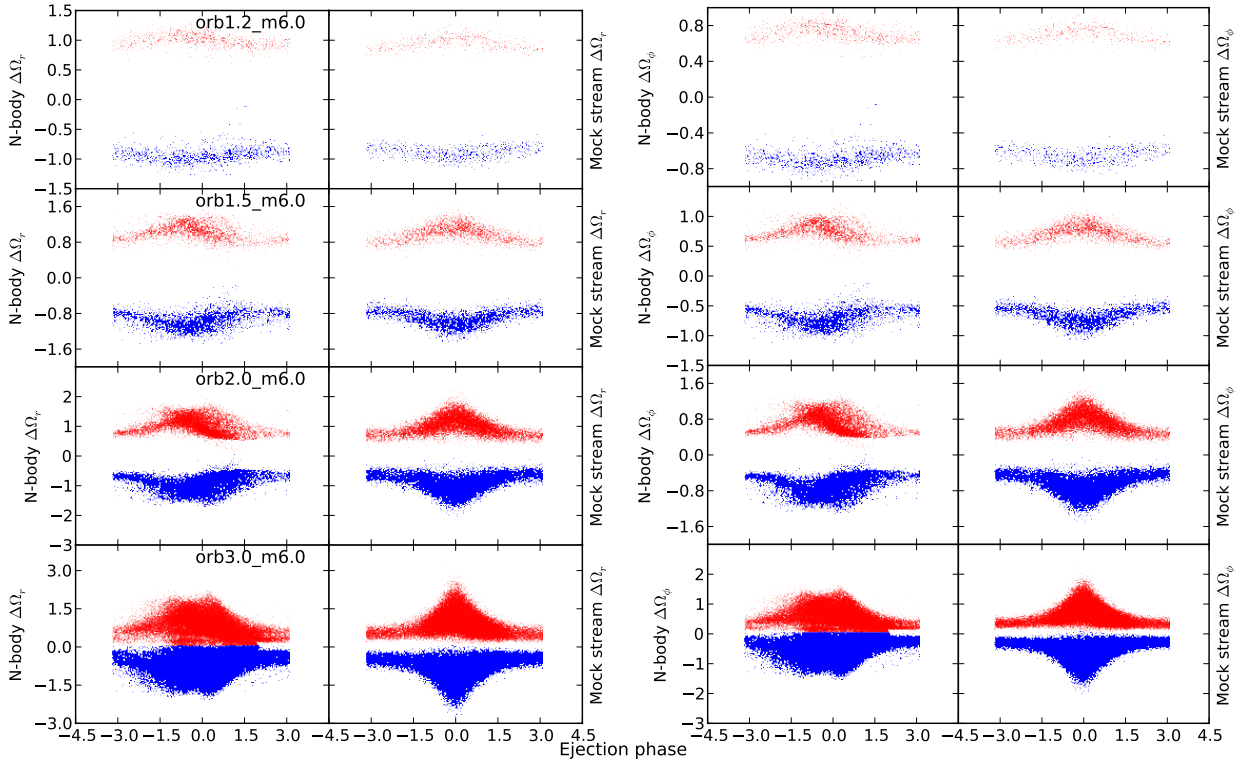
Figure 5 – *continued*

Figure 6. Orbital frequencies of stream stars. First two columns show Ω_r , second two show Ω_ϕ . These are given in units of radians / Gyr. In each pair of columns, simulation results are on the left and results from the mass loss model on the right.

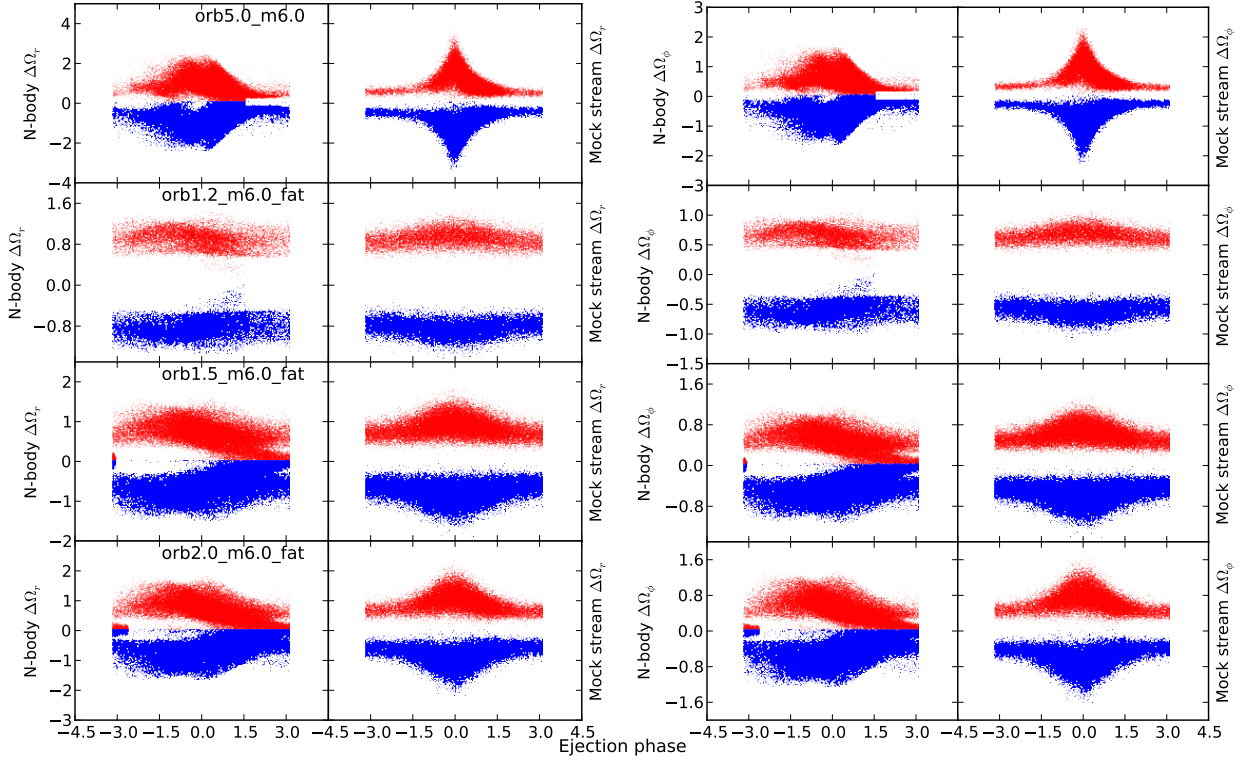


Figure 6 – continued

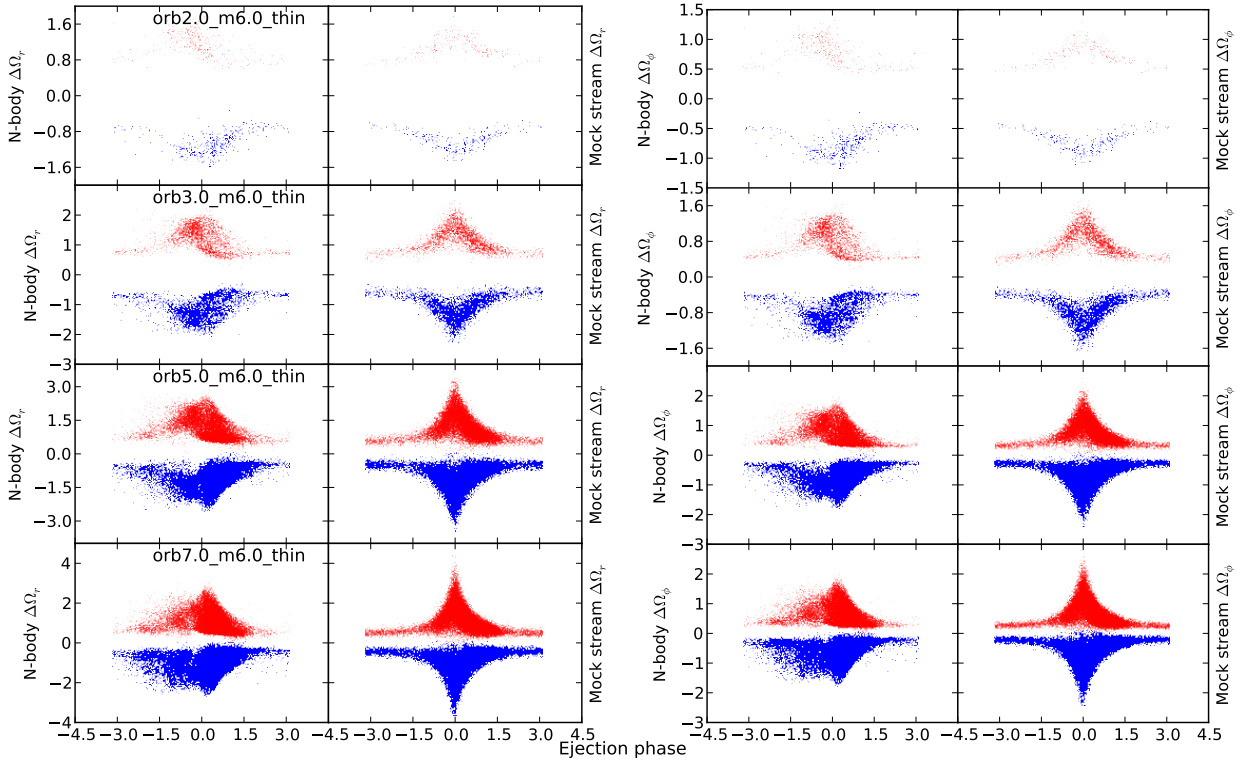


Figure 6 – continued

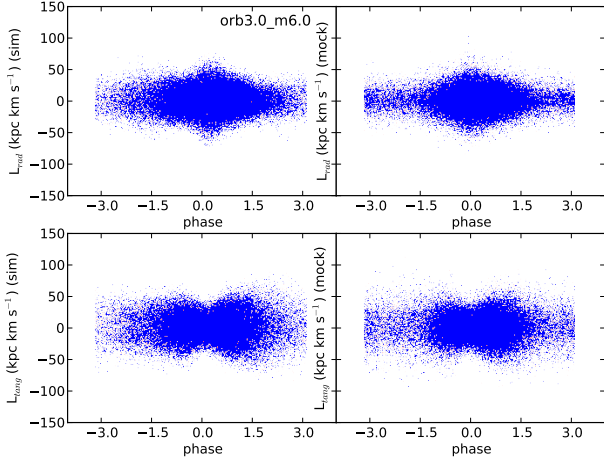


Figure 7. Angular momentum components in orbital plane, used as indicators of off-plane motions of the particles, shown as a function of ejected phase. First two columns show the component along the radial vector to the satellite, while the second two show the component along the tangential vector. In each pair of columns, simulation results are on the left and results from the mass loss model on the right.

release conditions is *not* constant, but decreases significantly for simulations with little mass loss (those on near-circular orbits). We address this by choosing dispersions $\sigma(k_r)$ and $\sigma(k_{v\phi})$ of the form

$$\sigma(k_r) = \sigma(k_{vt}) = \min(0.15 f_t^2 R_{acc}^{2/3}, 0.4) \quad (21)$$

The initial conditions for the particle-spray models in these and subsequent figures include these dispersions.

We also introduce a random nonzero offset in the off-plane position and velocity. For spherical simulations, this is necessary if we are to prevent the model stream from being entirely flat, in contrast to the simulation results. In a non-spherical potential, the vertical extent also thickens due to differences between Ω_z and Ω_ϕ . We choose $\sigma(k_z)$ and $\sigma(k_{vz})$ to reproduce the dispersion in the off-plane components of angular momentum along the radial and tangential vectors to the satellite at the time of ejection. In our model given by equations 7–8, these two components are determined by k_z and k_{vz} respectively. The choices

$$\bar{k}_z = \bar{k}_{vz} = 0 \text{ (by symmetry)} \quad (22)$$

$$\sigma(k_z) = 0.5 \quad (23)$$

$$\sigma(k_{vz}) = 0.5 \quad (24)$$

seems to reproduce the simulation results adequately, at least to the level we are interested in here (see Figure 7).

To generate a mock stream, we randomly sample the values k_r , $k_{v\phi}$, k_z , and k_{vz} from Gaussian distributions with the specified mean and dispersion. We can then determine the positions and velocities using equations 3–8 and 19–20 and then determine the actions (Figure 5) and frequencies (Figure 6) for each of our ejected particles. These figures were used to guide our choice of constants. The action plots of the simulations show a significant amount of interesting structure in some cases, in contrast to the particle-spray model which is fairly symmetrical about the origin and uni-modal at any ejection phase. However, the structure in the

frequency plots appears overall less complicated and more similar to the particle-spray model, though in some cases bi-modal structures or sprays of particles are still evident. The frequencies influence the stream properties more than the actions, so this is an encouraging sign for the particle-spray model.

The correlation between the angular momentum and radial action of the stream particles can be seen in the second and fourth rows of Figure 8. Here the first column is the simulation results, the second is the result of our recipe, while the third and fourth columns will be discussed later. It can be seen that our recipe reproduces the characteristic “bow-tie” pattern noted for this plot in this previous work (Eyre & Binney 2011; Bovy 2014).

Once we have chosen ejection times and phase-space coordinates for all the mock stream particles, we can evolve them through time either by direct orbital integration or by using the action-angle formalism. We use the latter method here because of the ease of action-angle calculations in the isochrone potential. We propagate the angles to the final timestep using the computed frequencies of each particle. Finally, we can determine the position and velocity of each particle by inverting the real-space to action-angle transformation. The results are shown in Figure 9. The agreement is quite impressive overall, showing deviation from the orbit by the correct amount and a fairly good agreement on the length, width, and surface brightness of the stream. The main deviations from the simulation can be found very close to the satellite and in the extreme tails of the distribution, but a careful inspection is necessary to find these differences.

5 STREAM GENERATION MODEL IN PRACTICE

5.1 Comparison of stream recipes

In Figure 8, we compare the results of our recipe to two other recipes that have appeared recently, which we implemented to the best of our understanding. The results of the simulations and our recipe appear in the first and second columns respectively. The Gibbons et al. (2014) recipe, which they call the “Lagrange Cloud stripping” method, appears in the third column, though in this case we are *not* including an additional force from the satellite as they found necessary, but simply integrating particles in the host potential. Also, here we take the velocity dispersion at particle release to be $\sigma_v = V_c(r)r_t/r$, which we found to be obeyed reasonably accurately by measuring the actual 1-d velocity dispersion of bound particles over our ensemble of simulations. In the Gibbons approach this dispersion is a free parameter used in fitting the results of simulations or observations. The recipe of Bonaca et al. (2014), which they call the “Fast-forward” method, appears in the fourth column. Both these recipes require an estimate for the velocity dispersion, but this is taken to be a free parameter used in fitting in the Gibbons approach.

For the two simulation cases shown, the Gibbons recipe results in frequency offsets that are generally too small. This agrees with their finding that the streams are too short without an additional force from the satellite. In contrast, the scale of the offset in the Bonaca recipe is fairly good.

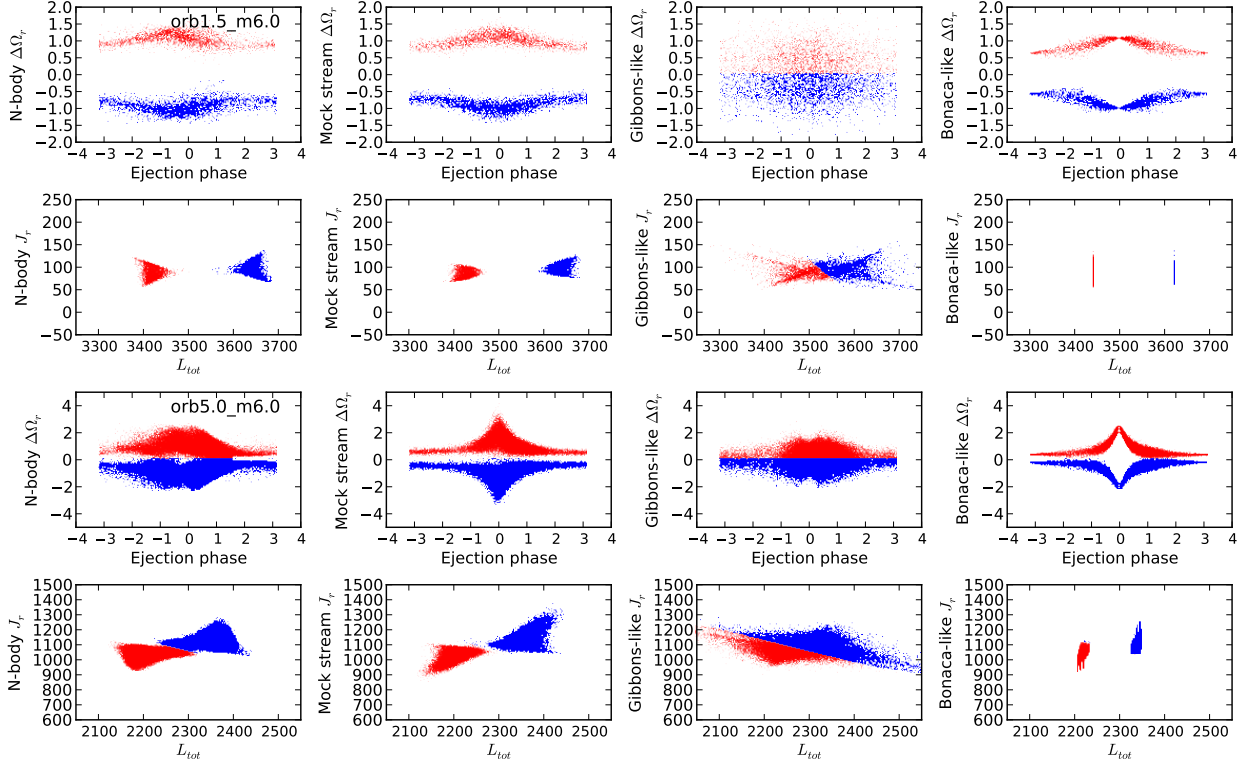


Figure 8. Comparison of different algorithms. The first two and second two rows use the `orb1.5_m6.0` and `orb5.0_m6.0` runs respectively. The first row for each run shows the radial frequency offset versus ejection phase. The second row for each run shows the radial action versus the angular momentum. The first column shows the simulations, the second our recipe, the third the Gibbons et al. (2014) recipe (minus the force from the satellite), and the fourth the Bonaca et al. (2014) recipe.

However, the contrast between minimum and maximum frequency is somewhat too large.

The Gibbons streams have frequency distributions that are too broad, especially for the first run shown ($r_a/r_p = 1.5$), so that the leading and trailing streams merge into each other. The especially narrow simulated frequency distribution in the first instance is evidence for the need to limit the ejected dispersion for nearly circular orbits. This plot shows the result when we take σ equal to the velocity dispersion of the satellite. In the Gibbons recipe, σ is actually treated as a free parameter. So in their approach the optimization should eventually pick a reasonable dispersion, but at the cost of losing any information obtainable from linking the release velocity dispersion to the satellite properties.

The Bonaca streams in contrast have a large radial action dispersion, but almost no dispersion in angular momentum, owing to the inclusion of dispersion only in the radial velocity. For certain simulations (see the lowest row in Figure 8), the dispersion is large enough to throw some stars backwards into the stream emerging from the opposing Lagrange point. This results in two extra streams emerging from the satellite in these cases. For most simulations, the frequency dispersion is too small at pericenter, which results in streaky features that are too short compared to the simulations. In summary, our recipe seems to improve the overall agreement with simulations compared to previous recipes for the cases examined here, though the differences will be more visible in some cases (mainly those with particularly small

or large eccentricities) than in others. The general similarity, along with the agreement with simulations we demonstrated in section 4, supports the general approach of particle-spray methods as used here and in the work of Gibbons et al. (2014) and Bonaca et al. (2014).

Turning now to the overall ensemble of simulations, the model streams shown in Figure 9 agree extremely well with the simulation results. The width, length, and substructure within the streams are all quite well reproduced. The most common deficiency is an excessively long tail of debris, which stems in part from our use of simple Gaussian distributions of the space and velocity offsets rather than a more sharply truncated distribution.

5.2 Different host potentials

To extend the test of the method beyond the parameter range where it has been calibrated, we run an N -body simulation based on the one shown in Figure 2 of Gibbons et al. (2014). This simulation uses a different potential and a much more massive satellite than those we have examined so far. The host potential for this run is a spherical Navarro-Frenk-White profile, with a mass of $7.5 \times 10^{11} M_\odot$ contained within a radius of 185.41 kpc, and a scale radius of 9.27 kpc yielding a concentration of 20. This equates to a virial overdensity of 180 with respect to the critical density for a Hubble constant of $H_0 = 75 \text{ km s}^{-1}$. We use a $W = 3$ King model of $6.4 \times 10^8 M_\odot$ and outer radius 4.75 kpc. We set this moving

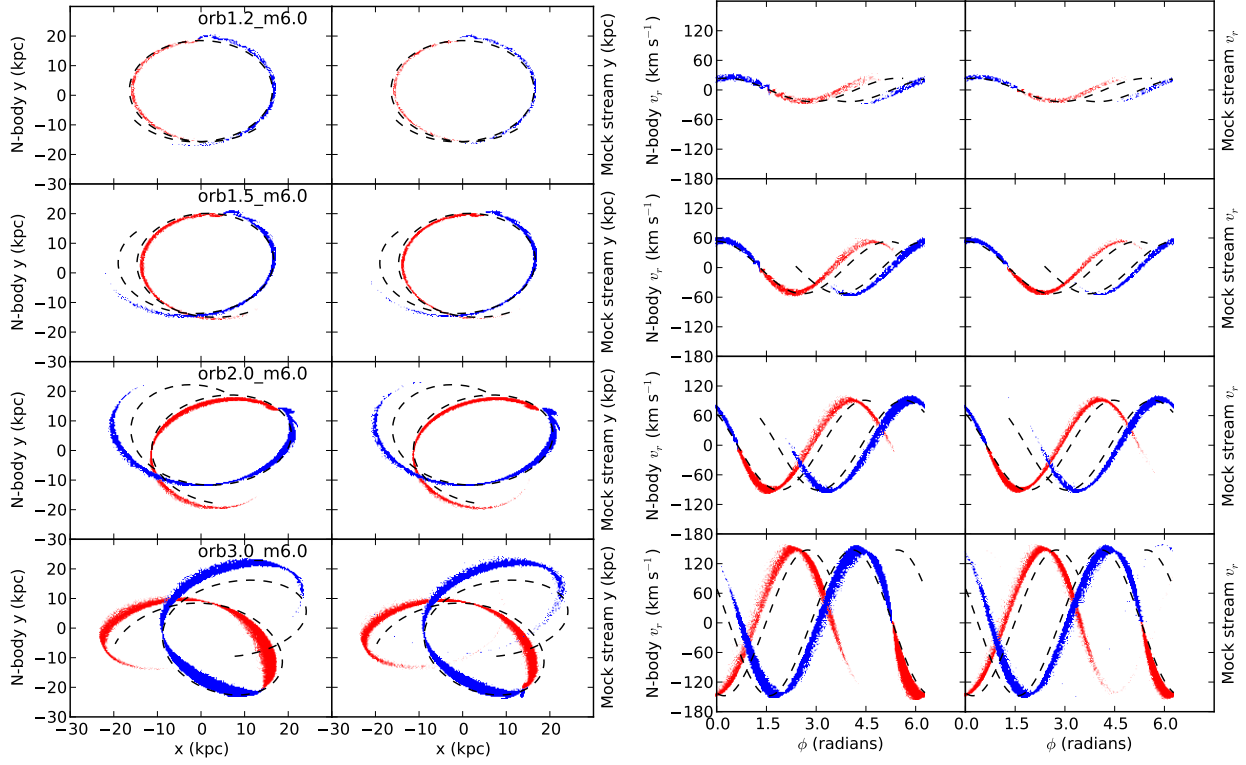


Figure 9. Stream position / velocity. First two columns show a face-on view of the orbit plane, while the second two show the radial velocity versus the azimuthal angle. In each pair of columns, simulation results are on the left and results from the mass loss model on the right. Streams are shown at the last apocenter timestep at which the satellite is still intact.

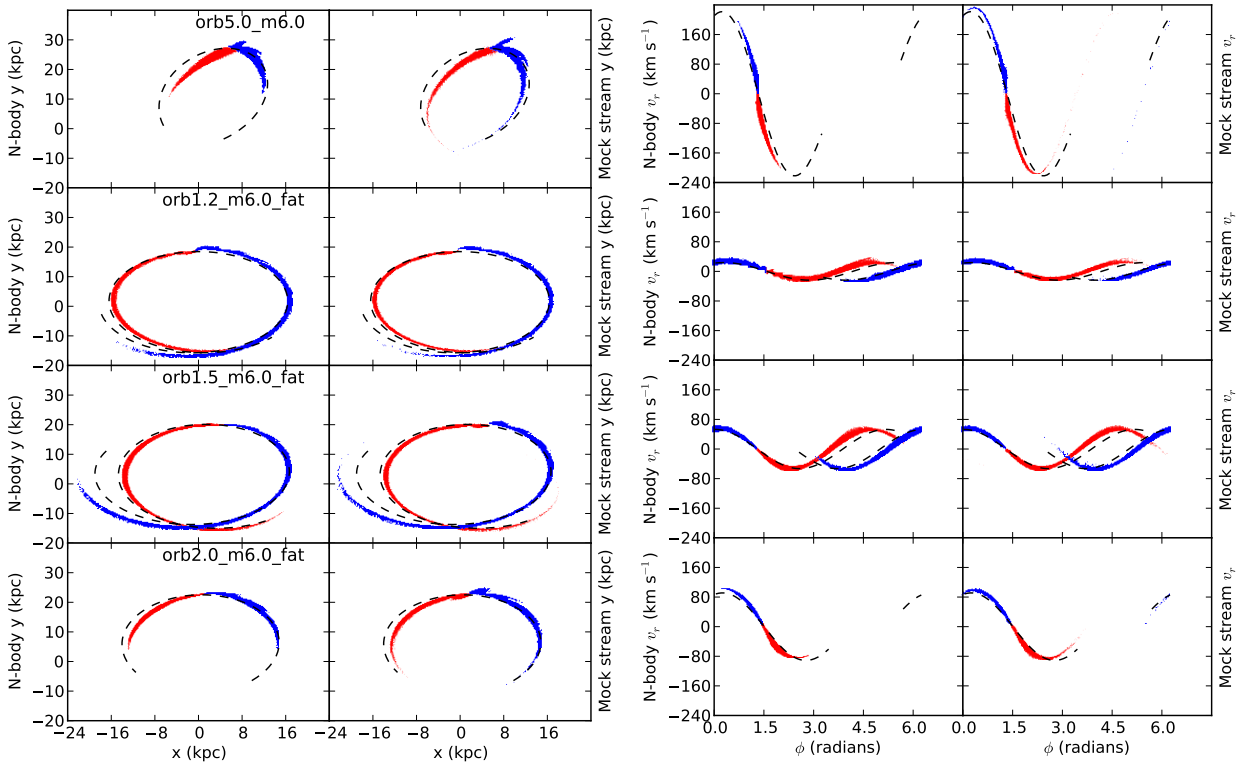


Figure 9 – continued

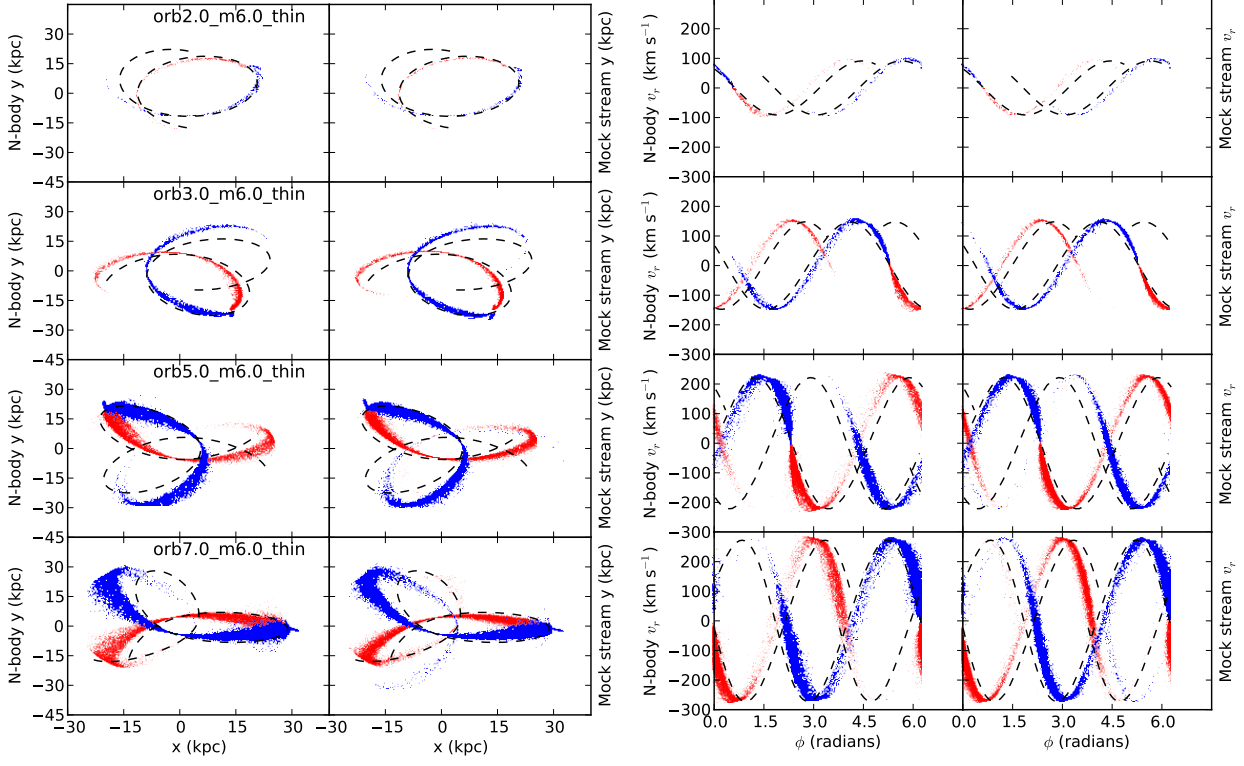


Figure 9 – continued

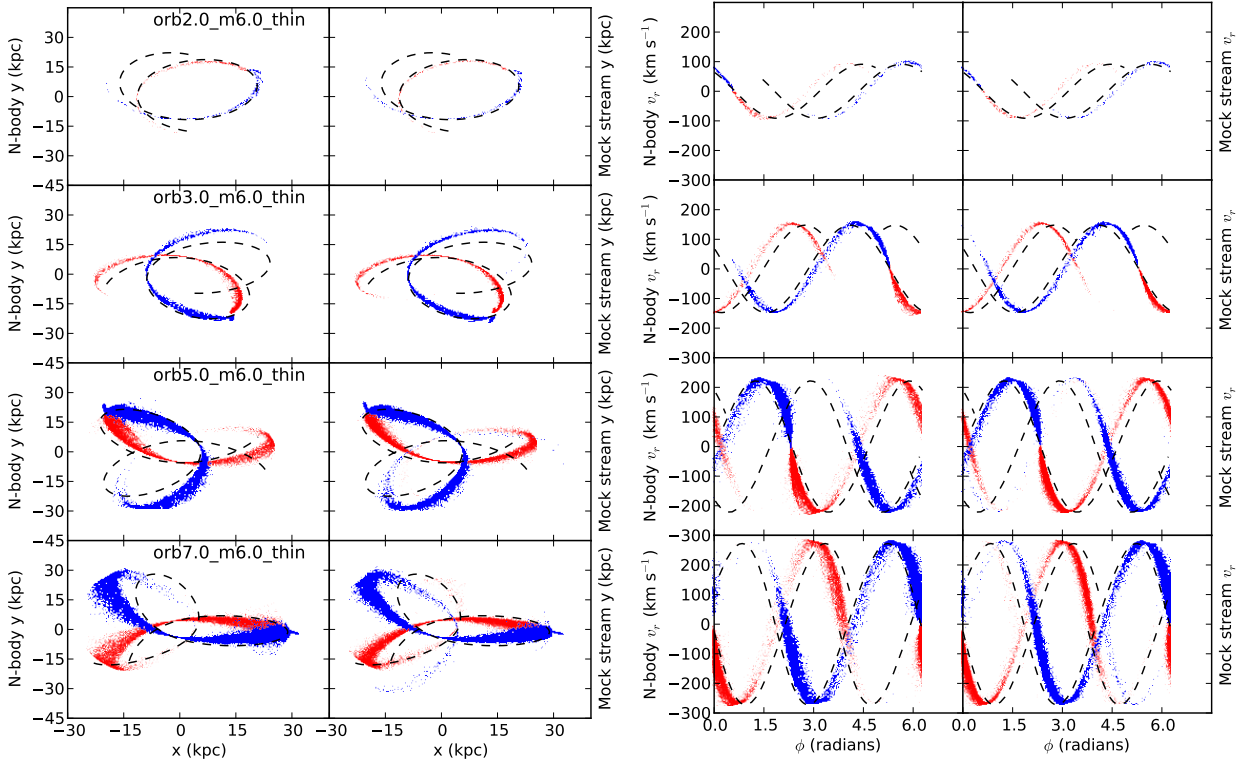


Figure 9 – continued

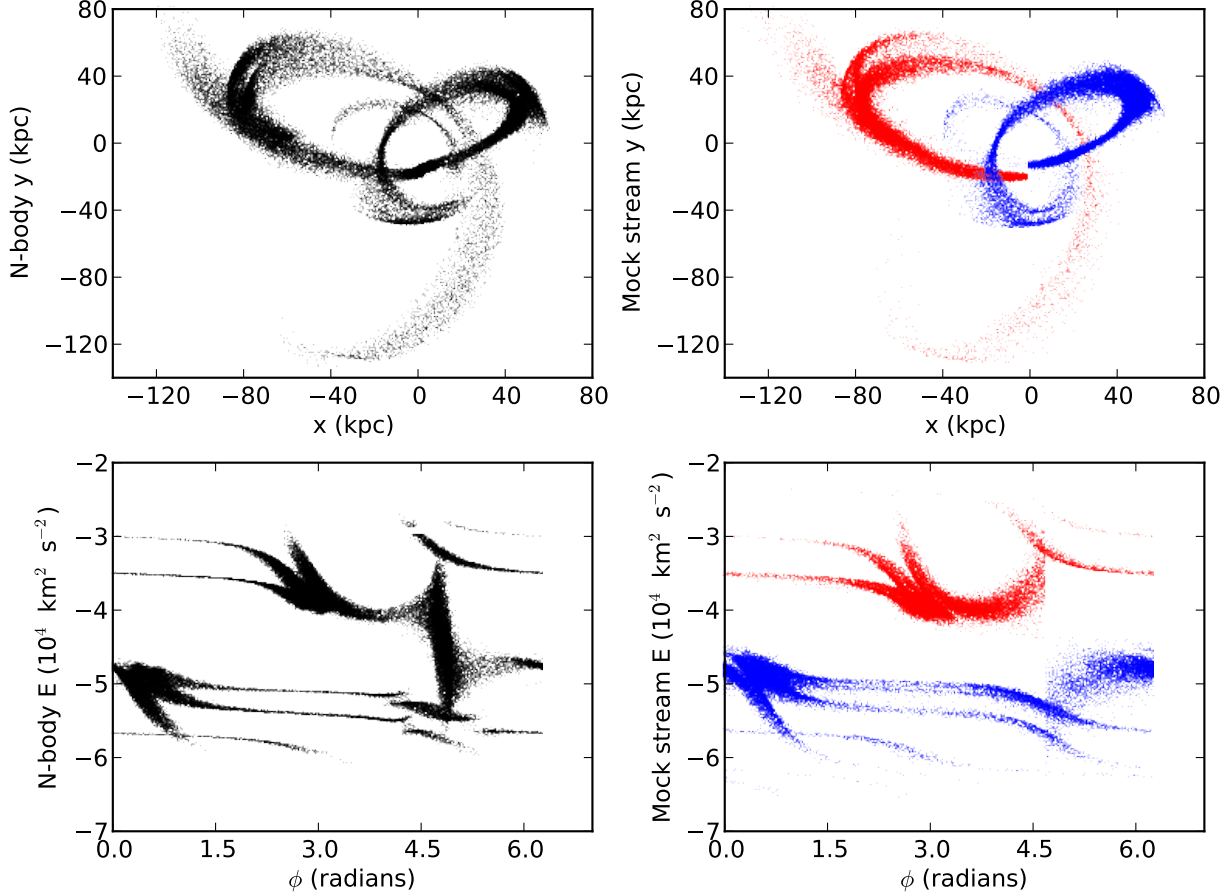


Figure 10. *N*-body simulation roughly emulating the Sagittarius stream (left column), following Gibbons et al. (2014), and particle-spray model thereof (right column). The top row shows particle positions. The bottom row shows the particle energies versus azimuth; streams from different pericenter passages are particularly well separated in this representation. The progenitor appears at $x = 0$ kpc, top left vertical streak in The complex structure of the simulated stream is well reproduced by the particle-spray model.

in the x - y plane with coordinates $x_0 = -2.327$ kpc, $y_0 = 70.772$ kpc, $v_{x0} = -78.71$ km s $^{-1}$, and $v_{y0} = -2.59$ km s $^{-1}$. The resulting orbit has apocenter 70.8 kpc and pericenter 17.8 kpc, and combining this orbit with the satellite properties leads to a tidal factor $f_t = 0.8$.

The simulation results are shown in the left column of Figure 10, at a time 4.14 Gyr into the run. At this point the satellite is just past the fourth pericenter, so three separate streams from previous pericentric passages are clearly visible in both the leading and trailing streams. The spatial distribution of the particles is similar to that of Gibbons et al. (2014). The different streams separate particularly well in the lower row, which shows the particle energies plotted versus azimuth. In the spatial distribution, these streams separate most clearly at apocenter of the radial loops. This substructure clearly shows the action-angle tilt which is expected to dominate for a young stream (only 3.5 radial oscillations), as discussed above.

Results from our particle-spray model are shown in the right-hand column. We have performed the required orbit integrations using the `galpy` package written by Jo Bovy. Clearly, the complex structure of the stream is well reproduced by our model. When overlaid, the multiple compo-

nents of the leading and trailing streams match the *N*-body model nearly exactly. Some slight differences are visible, notably gaps at two different azimuth values in the leading stream of the simulation and one in the leading stream in the energy plot. One of these gaps is also visible in the spatial distribution, and results in a “C”-shaped feature separated from the rest of the leading stream. These features result from the satellite crossing its own stream, as made inevitable by the perfectly spherical potential used here, and creating a gap in the manner studied by Carlberg (2013). Since our model does not include the satellite potential, these gaps do not appear in the right-hand column. The model stream is somewhat longer and in some places narrower than the *N*-body results. Also, differences are easily apparent near the progenitor satellite, both from the progenitor itself (not represented in the particle-spray model) and from particles that have been stripped but have yet to acquire their full action offset as they curve away from the progenitor. Overall, however, the agreement is extremely good.

Figure 11 shows the performance of the particle spray recipe in a compound bulge-disk-halo potential. Two orbits are shown, one on a regular orbit and one on a mildly chaotic orbit. The satellite in this test is located at a po-

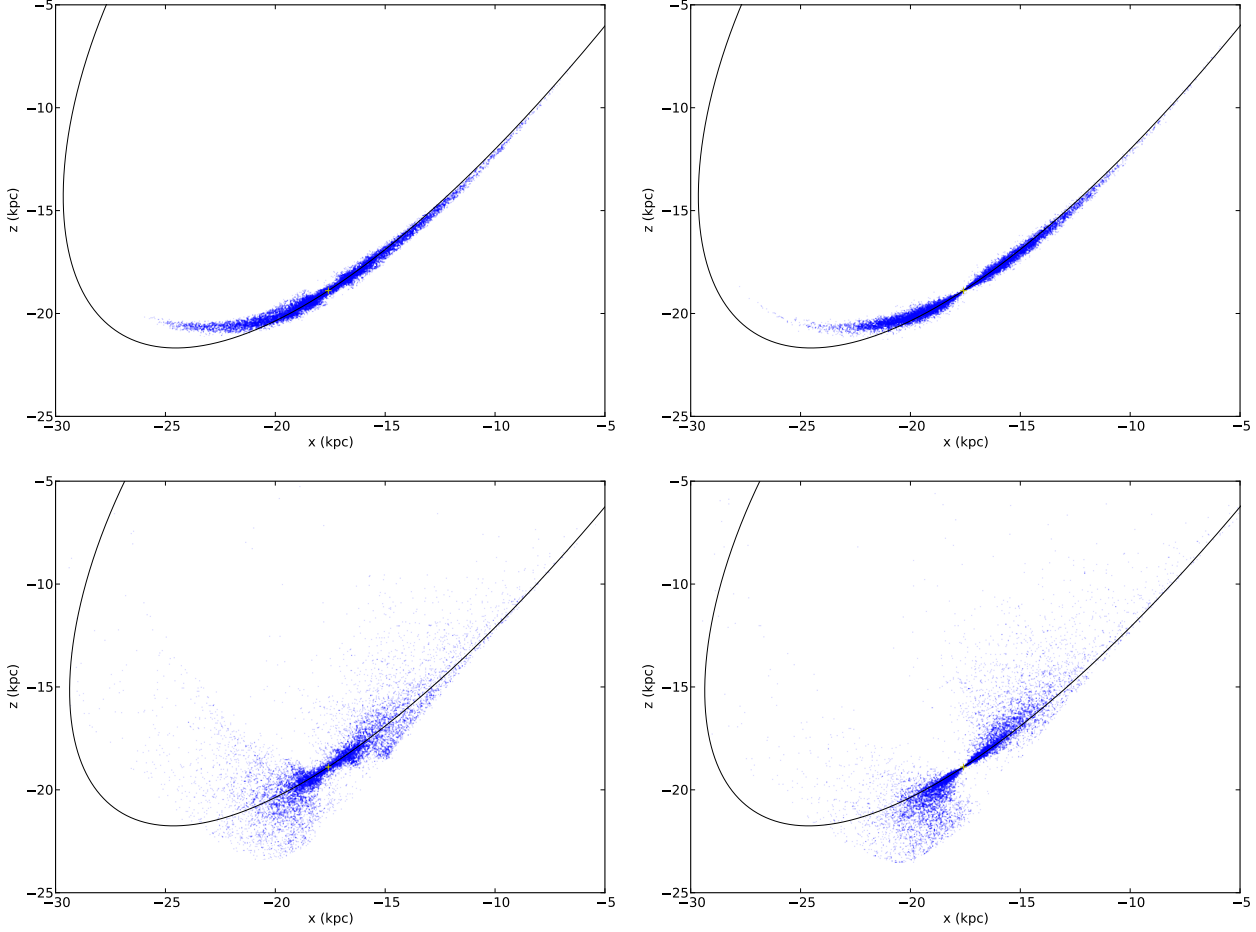


Figure 11. Simulations using a bulge-disk-halo potential, as discussed in the text. Left columns: N -body simulations. Right columns: particle-spray models. Upper row: regular orbit with $q = 0.57$. Lower row: apparently chaotic orbit with $q = 0.60$.

sition $x_0 = -17.59$ kpc, $y_0 = -10.55$ kpc, $z_0 = -18.89$ kpc and velocity $v_{x0} = -119.8$ km s $^{-1}$, $v_{y0} = 24.36$ km s $^{-1}$, and $v_{z0} = -83.12$ km s $^{-1}$. We initialize the satellite with mass $4 \times 10^4 M_\odot$ and tidal factor $f_t = 0.7$. The orbit is integrated backwards from the given point for $t_d = 2694$ Myr, and then the particle-spray and N -body simulations are evolved to the present day. In the fixed potential used here, the bulge is a Hernquist profile with mass $3.4 \times 10^{10} M_\odot$ and radius 0.7 kpc. The disk is a Miyamoto-Nagai disk with mass $10^{11} M_\odot$, $a = 6.5$ kpc, and $b = 0.26$ kpc. The halo is an oblate logarithmic halo with $\phi(R, z) = V_h^2 \ln(R^2 + (z/q)^2 + d^2)$, $V_h = 115$ km s $^{-1}$, and $d = 12$ kpc. The only difference between the orbits used in the top and bottom rows is that the top uses $q = 0.57$, and the bottom $q = 0.60$.

The thickness of the streams in the top and bottom rows differs markedly, for both the particle-spray models and N -body simulations. This appears to be due to the nature of the progenitor orbits. The orbit in the top case is regular, as we verified using a Poincaré surface of section plot. In contrast, the surface of section for the bottom case is slightly thickened, indicating a small degree of chaos. If we further increase the flattening parameter to $q = 0.63$, the orbit becomes regular again, and in tandem the stream becomes narrow again so that it much more closely resembles the top panel. (Admittedly, the flattening in all of these halo poten-

tials is perhaps unrealistically high, but chaotic orbits can be found in more realistic potentials as well, as in Hunter 2005.) It is worth noting that in this case, the thickening of the stream arises within less than five radial oscillations. Long integration times are apparently not required to see the influence of chaos on tidal streams.

The results in Figure 11 demonstrate we can obtain reasonable results from the particle-spray model, even when the progenitor orbit is irregular, though some areas of disagreement can be found in both rows. In fact, having first noticed a highly thickened stream in a similar orbit and potential using the particle-spray model, we suspected a bug in our code until the N -body model demonstrated the same behavior. For the spray model to work on a chaotic orbit, the particle coordinates must be evolved by direct orbit integration rather than by using an action-angle formalism.

The fraction of orbits exhibiting chaotic behavior is generally small, though nonzero, in the idealized axisymmetric models often used in stream modeling (Hunter 2005). However, the fraction of orbits demonstrating chaotic behavior in *realistic* galaxy potentials, which include triaxiality, radial shape dependence, time dependence, and substructure, may well be higher. Also, real galaxy potentials and hence the orbits within them evolve with time. In principle, orbits may sweep through chaotic regions, puffing up their

streams. This would raise the fraction of tidal streams affected by chaotic behavior beyond the fraction of orbits that are currently chaotic.

In this last set of simulations, we chose the parameters such that the satellite remains partly intact until the end of the simulation. If the satellite is more diffuse, it comes apart earlier in the N -body run than in the particle-spray model. Presumably this is due to disk shocking, though we have not investigated the cause in detail. The particles are also spread more evenly along the stream than in the particle-spray model, where there tends to be a central hole. These discrepancies join those mentioned earlier as the main discrepancies with the N -body results: differences in the tails of the particle distributions, inaccuracy in the satellite mass as a function of time, and inaccuracy of the streams near the satellite Lagrange points. However, overall the agreement between these two methods is impressive, suggesting the stream recipe is suitable for fast modeling of streams in a Bayesian context.

6 DISCUSSION

We have presented a recipe for modeling tidal streams without the cost of a full N -body simulations. The typical computation times are a few minutes, as opposed to a typical computation time of six hours for the N -body runs in Table 1. This recipe has many similarities with recent suggestions by Gibbons et al. (2014) and Bonaca et al. (2014), but differs in several respects. Here we discuss some aspects of our recipe in the context of these and other methods.

Our method clearly reproduces the differences between the stream and the orbit that were reviewed in Section 2.2. As discussed in that section, the stream behavior is determined primarily by the distribution of orbital frequencies (or equivalently the actions) upon release. Even though we have made simplifying assumptions about the way the stars are released, and neglected the subsequent influence of the satellite, the behavior of streams is still remarkably faithful to the N -body results.

Our model also reproduces the dispersion along various dimensions of the stream fairly well. Streakline techniques such as those of Varghese et al. (2011) or Küpper et al. (2012) by design do not model this dispersion. Therefore, they fail in particular to reproduce the portions of the stream furthest from the satellite, which are dictated by the extremes of the frequency distribution at the first disruptive pericenter. They similarly fail to reproduce the extent of any other lobes or streaky features within the stream. Thus while they are certainly easier to compute, the folded streaklines evidenced by Küpper et al. (2012) are not necessarily easier to fit to the stream than a full particle distribution. In addition, the length and width of the stream contains useful information on the satellite mass and overall duration of the disruption process. These parameters are in turn valuable in obtaining a more accurate fit to the orbit and the potential.

Substructure in streams provides important constraints, as described in section 2.3 and further illustrated in section 5. A crucial point in modeling these streams is that the actions and frequencies of released stars must vary over the radial cycle. In the recipe of Bovy (2014) for example, the distribution of actions and frequencies is assumed constant.

This type of model is useful in modeling old streams where the substructure overlaps, but is unable to reproduce the complex spatial pattern seen in for example Figure 10. The ejection recipe in our model naturally reproduces the variation in orbital properties. In principle, this variation can be incorporated into action-angle stream models as well, which would be useful in obtaining large particle numbers (or accurate stream distribution functions) at a fixed computational cost.

While an action-angle approach has important advantages, irregular orbits will pose a problem for this approach. For these orbits, directly integration of the orbits as we have done here seems the only viable method. The results shown in Figure 11 suggest that chaotic orbits result in puffed-up streams within a few orbital times. Further investigation into the effects of chaos on realistic galactic potentials and tidal streams within them seems warranted.

Our model has a varying emission rate peaking near pericenter, in contrast to the constant emission used by Bonaca et al. (2014) and Bovy (2014) among others. We have tested the effect of a uniform emission rate versus the simulation in Figure 10. The effects are more subtle than those of the oscillating actions and frequencies; the substructure is still easily visible. However, the influence of the emission rate is still evident in the abundance of particles between the clearly separated streams, which fill in the distinct shells seen at apocenter of the radial loops and blur the separate streams visible in the energy plot. Thus this effect too is important in modeling streams with visible substructure.

Our model also explicitly takes into account the decrease of the satellite mass with time. This improves upon the treatment in the models of Gibbons et al. (2014) and Bonaca et al. (2014), as well as the earlier streakline models, where the mass is assumed fixed. Models with multiple interactions can be modeled fairly accurately with our simple assumptions, as long as the satellites and orbits resemble those used in our tests. For less disruptive encounters, more careful modeling of the tidal excitation is probably necessary. Very disruptive encounters will require a criterion for total disruption and a prescription for the particles ejected at that point. Including a disk in the host potential could lead to disk shocking and a more rapid mass loss than specified by our current recipe. Finally, different satellite profiles will probably require a recalibration of the mass loss prescription. As discussed above, previous work has shown that satellites with various density profiles evolve in a predictable manner during moderate rates of tidal stripping, so this recalibration should be possible as long as the satellites are dynamically hot systems. The mass evolution in turn affects the actions and frequencies of released particles, and ignoring it in the case of Sagittarius for example may lead to significant biases.

When compared to the Bonaca et al. (2014) method, two more differences stand out. First, they release stars at the angular velocity of the satellite, which results in a larger oscillation of actions and frequencies over the radial cycle than in our equations 6 and 20. Second, they blur the release velocity of the satellite by the velocity dispersion in the satellite, which in many cases is a larger dispersion than we use. In some cases their assumptions work well, but in cases with small or large eccentricities we find that they can produce streams that are too smeared out in azimuth or radius.

The streams in Bonaca et al. (2014) are both produced and analyzed with the same method, so it is unclear whether these assumptions have much effect on the larger conclusions in their paper. Still, these differences are only strongly evident in certain situations. Overall, our results strongly validate their general approach of modeling particle sprays using orbits in the host potential alone.

The method of Gibbons et al. (2014) is somewhat different, in that they include an ongoing force from the satellite in calculating the particle evolution. It thus closely resembles a standard restricted N -body method. (A simple alternative to their method is to run a restricted N -body simulation after first removing the central particles of the progenitor, because they remain bound to the satellite and add nothing but computation time.) In their runs, between a quarter and a half of the released particles are recaptured by the satellite and later released in bursts at pericentric passage. Our method has the advantage that we do not need to calculate the evolution of these recaptured particles, which require short timesteps compared to the freely moving stream particles. Gibbons et al. (2014) find that the force from the satellite must be included. However, we find that it can be omitted with an appropriate choice of release constants (equations 19–24); the time-integrated effect of the progenitor is encapsulated by our larger action offset. One can then use a simpler, general-use package for calculating the orbital evolution, rather than more specialized codes. In our case we have used the `galpy` package which contains a large assortment of potentials when orbit integrations are required.

Another difference is that our method prescribes the rate of particle release as a function of orbital phase. While this form may not be completely accurate, it is unclear whether the alternative of using recaptured particles to generate bursts biases the results in some way. Finally, the velocity dispersion of released particles is prescribed by our recipe, and tied to the satellite mass and other parameters of the problem, where in Gibbons et al. (2014) it is taken to be a free fitting parameter. Our method thus discards less information, in principle increasing the statistical power of the fit. The main advantage of the Gibbons et al. (2014) method is the automatic inclusion of multiple interactions between the satellite and its stream, which can create stream gaps like those visible in Figure 10. Also, at very large satellite masses the effect of the satellite will not converge within an orbital wrap and this will alter the morphology of the tidal stream (Choi et al. 2007), making explicit inclusion of the satellite force necessary.

Of course, one may question to what extent the idealized N -body simulations used in this paper reflect the cases expected in reality. Bonaca et al. (2014) describes an interesting experiment, where streams were generated in both fixed potentials and in a cosmological simulation of a halo, and then fitted to constrain a parameterized model of the dark matter halo. While the fixed potential streams consistently returned accurate results, the cosmological halo streams yielded highly biased or imprecise results in many cases. Bonaca et al. suggest the differences arise from gradual evolution in the potential, interaction with subhalos, and deviations of the true potential shape from the fitted form. We also note the effect of chaotic orbits, as in Figure 11 above, may play a role in these differences. There

are some reasons to think the results of Bonaca et al. are too pessimistic about the scientific yield from studying tidal streams. Neither of the two “streams” displayed from their much larger sample particularly resembles prominent Milky Way streams in the cosmological case, while one of them does not look much like a stream in the fixed-potential case either. We suggest that in the outer halo, progenitors that are more massive than the globular-like systems they employ (mass of $2 \times 10^4 M_\odot$) are necessary in order to generate streams that yield robust measures of the potential. (The fixed-potential case does yield good results, but this presumably depends on the assumption of perfect six-dimensional observational data.) This would align with earlier work using more massive progenitors (Siegal-Gaskins & Valluri 2008), which found only minor effects of substructures on tidal streams. Still, the analysis of Bonaca et al. (2014) raises interesting challenges to the project of stream fitting, and further work on how to interpret and combine results from individual stream fits is clearly required.

To the challenges facing stream models, we may add the issue of dynamical friction. Stream models are often initialized with a satellite at a particular place and time, usually a particular pericentric passage. Dynamical friction is frequently invoked as a way of bringing this satellite onto its destructive orbit, but it is then often neglected in the actual calculation of the stream, or else applied only to the satellite but not the stream. Full N -body simulations with a live host can implement dynamical friction accurately. However, this technique is extremely expensive, since high particle numbers are necessary to suppress the effects of particle noise. Thus at this point, a good technique for incorporating dynamical friction consistently in stream models has yet to be introduced.

7 CONCLUSIONS

In summary, we have presented and tested a recipe for modeling tidal streams as a collection of particles, released and evolved in the host potential *without* the added influence of the progenitor satellite. This recipe includes a prescription for calculating the mass lost from the progenitor, and thus the mass in the tidal stream as well. The mass loss and orbital properties of the debris both oscillate with the satellite position, producing substructure within the tidal stream. The recipe assumes hot, compact one-component progenitors, and will require adaptation for more complicated cases, or orbits very different from the moderately disrupting cases examined here.

The intended use of this recipe is for Bayesian sampling, which requires a very large number of trial models to obtain accurate constraints on parameters. The particle-spray method adds one more arrow to the quiver for those seeking to use tidal streams to obtain physical insights. The observational situation has been developing rapidly. Numerous streams have been found in the Milky Way using the Sloan survey, and in M31 with the PAndAS survey. New techniques have revealed tidal streams in more distant galaxies with even modest-sized telescopes, and kinematic tracers have been demonstrated in some of these streams as well. Forthcoming results from Pan-STARRS and Gaia, among other surveys, should transform the field of tidal streams into

a high-precision industry. We expect particle-spray modeling such as that tested here to be one of its chief tools.

ACKNOWLEDGMENTS

We thank Tom Quinn and Joachim Stadel for the use of PKDGRAV, and Josh Barnes for the use of ZENO. We thank Jo Bovy for making public the `galpy` package and assisting with its use. We also thank Jo Bovy and Aaron Romanowsky for interesting discussions of tidal stream physics and observations. MAF, MDW, and SH acknowledge support by NSF grant AST-1009652 to the University of Massachusetts. MDW also acknowledges the support of NSF AST-0907951.

REFERENCES

- Aarseth S. J., Heggie D. C., 1998, *MNRAS*, 297, 794
- Belokurov V., Zucker D. B., Evans N. W., Gilmore G., Other S., Authors D. M., 2006, *ApJ*, 642, L137
- Binney J., Tremaine S., 2008, *Galactic Dynamics: Second Edition*. Princeton University Press
- Bonaca A., Geha M., Kuepper A. H. W., Diemand J., Johnston K. V., Hogg D. W., 2014, *ArXiv e-prints*
- Bovy J., 2014, *ArXiv e-prints*
- Carlberg R. G., 2013, *ApJ*, 775, 90
- Chernoff D. F., Weinberg M. D., 1990, *ApJ*, 351, 121
- Choi J.-H., Weinberg M. D., Katz N., 2007, *MNRAS*, 381, 987
- Eyre A., Binney J., 2011, *MNRAS*, 413, 1852
- Fardal M. A., Babul A., Gehan J. J., Guhathakurta P., 2006, *MNRAS*, 366, 1012
- Fardal M. A., Weinberg M. D., Babul A., Irwin M. J., Guhathakurta P., Gilbert K. M., Ferguson A. M. N., Ibata R. A., Lewis G. F., Tanvir N. R., Huxor A. P., 2013, *MNRAS*, 434, 2779
- Gibbons S. L. J., Belokurov V., Evans N. W., 2014, *ArXiv e-prints*
- Gieles M., Alexander P. E. R., Lamers H. J. G. L. M., Baumgardt H., 2014, *MNRAS*, 437, 916
- Gnedin O. Y., Ostriker J. P., 1997, *ApJ*, 474, 223
- Hayashi E., Navarro J. F., Taylor J. E., Stadel J., Quinn T., 2003, *ApJ*, 584, 541
- Heggie D. C., 2001a, in Steves B. A., Maciejewski A. J., eds, *The Restless Universe Escape in Hill's problem*. pp 109–128
- Heggie D. C., 2001b, in Deiters S., Fuchs B., Just A., Spurzem R., Wielen R., eds, *Dynamics of Star Clusters and the Milky Way* Vol. 228 of *Astronomical Society of the Pacific Conference Series*, *Mass Loss from Globular Clusters*. p. 29
- Helmi A., White S. D. M., 1999, *MNRAS*, 307, 495
- Howley K. M., Geha M., Guhathakurta P., Montgomery R. M., Laughlin G., Johnston K. V., 2008, *ApJ*, 683, 722
- Hunter C., 2005, *Annals of the New York Academy of Sciences*, 1045, 120
- Johnston K. V., 1998, *ApJ*, 495, 297
- Just A., Berczik P., Petrov M. I., Ernst A., 2009, *MNRAS*, 392, 969
- King I. R., 1966, *AJ*, 71, 64
- Küpper A. H. W., Kroupa P., Baumgardt H., Heggie D. C., 2010, *MNRAS*, 401, 105
- Küpper A. H. W., Lane R. R., Heggie D. C., 2012, *MNRAS*, 420, 2700
- Küpper A. H. W., MacLeod A., Heggie D. C., 2008, *MNRAS*, 387, 1248
- Lamers H. J. G. L. M., Baumgardt H., Gieles M., 2010, *MNRAS*, 409, 305
- Murali C., Weinberg M. D., 1997, *MNRAS*, 291, 717
- Odenkirchen M., Grebel E. K., Dehnen W., Rix H., Yanny B., Newberg H. J., Rockosi C. M., Martínez-Delgado D., Brinkmann J., Pier J. R., 2003, *AJ*, 126, 2385
- Peñarrubia J., Navarro J. F., McConnachie A. W., 2008, *ApJ*, 673, 226
- Price-Whelan A. M., Hogg D. W., Johnston K. V., Hendel D., 2014, *ArXiv e-prints*
- Sanders J. L., 2014, *MNRAS*, 443, 423
- Sanders J. L., Binney J., 2013a, *MNRAS*, 433, 1813
- Sanders J. L., Binney J., 2013b, *MNRAS*, 433, 1826
- Sanderson R. E., Helmi A., Hogg D. W., 2014, in Feltzing S., Zhao G., Walton N. A., Whitelock P., eds, *IAU Symposium* Vol. 298 of *IAU Symposium*, *Action-space clustering of tidal streams to map the Galactic potential*. pp 207–212
- Siegal-Gaskins J. M., Valluri M., 2008, *ApJ*, 681, 40
- Sohn S. T., van der Marel R. P., Carlin J. L., Majewski S. R., Kallivayalil N., Law D. R., Anderson J., Siegel M. H., 2014, *ArXiv e-prints*
- Takahashi K., Portegies Zwart S. F., 2000, *ApJ*, 535, 759
- van den Bosch F. C., Lewis G. F., Lake G., Stadel J., 1999, *ApJ*, 515, 50
- Varghese A., Ibata R., Lewis G. F., 2011, *MNRAS*, 417, 198